Chemical Engineering Journal 427 (2022) 132006

Contents lists available at ScienceDirect

Chemical Engineering Journal

journal homepage: www.elsevier.com/locate/cej

Visible-light driven sonophotocatalytic removal of tetracycline using Ca-doped ZnO nanoparticles

Alejandro Bembibre [a], Majdi Benamara [b], Mokhtar Hjiri [c], Elvira Gómez [a,*], Hatem R. Alamri [d], Ramzi Dhahri [e,*], Albert Serrà [a,*]

[a] Thin Films and Nanostructures Electrodeposition Group (GE-CPN), Department of Materials Science and Physical Chemistry, University of Barcelona, Martí i Franquès 1, E-08028 Barcelona, Catalonia, Spain
[b] Laboratory of Physics of Materials and Nanomaterials Applied at Environment (LaPhyMNE), Faculty of Sciences, University of Gabes, Erriadh Manara Zrig, 6072 Gabes, Tunisia
[c] Department of Physics, Faculty of Sciences, King Abdulaziz University, 21589 Jeddah, Saudi Arabia
[d] Physics Department, Al Jumum University College, Umm Al-Qura University, Makkah, Saudi Arabia
[e] Department of Engineering, University of Messina, 98166 Messina, Italy

ARTICLE INFO

Keywords:
Sono-photocatalysis
Water decontamination
Photocatalysis
Tetracycline

ABSTRACT

Highly efficient, long-term, eco-friendly catalysts for water decontamination technology are urgently needed to meet the prioritized objectives of green development and societies worldwide. Ca-doped ZnO was investigated as environmentally friendly sono-photocatalytic system under LED visible light irradiation to efficiently mineralize tetracycline-based antibiotics. The effects of pH, Ca doping, light, ultrasound, and pH on the mineralization of tetracycline by Ca-doped ZnO nanopowders and on the chemical, sono-, photo- and sono-photostability of Ca-doped ZnO nanopowders were systematically investigated. The ZnO-based catalyst with 2 at. % of Ca dopant exhibited the best sono-photocatalytic performance in mineralizing tetracyclines under visible LED light and ultrasound irradiation (i.e., ≥99% mineralization in 90 min), with excellent reusability and minimal sono-photocorrosion (i.e., ≤1% of catalyst dissolution in 180 min), which were even greater in the absence of organic pollutants and in the pH range of most natural waters. For Ca-doped ZnO nanopowders, the role of the generated reactive oxygen species under light and ultrasound stimulation and the mechanism of the mineralization of tetracycline were analyzed. In conclusion, the sono-photocatalytic mineralization of antibiotics synergizing visible LED light and weak ultrasound irradiation in the presence of Ca-doped ZnO nanopowders presents an outstanding start to developing highly efficient, long-term, eco-friendly catalysts for efficiently treating emerging organic pollutants.

1. Introduction

Only approximately 1.1% of all surface water worldwide is suitable for drinking, largely due to contaminants such as heavy metals, oils, organic products, and especially pharmaceutical compounds found in aquatic systems [1,2]. In particular, of the estimated 100000 to 200000 tons of antibiotics consumed in food animals worldwide each year, all of which are rarely metabolized in the body after consumption, 30% to 90% remain active after excretion and are continuously released into bodies of water, especially in developing countries, due to poor regulation, wastewater treatment, and management [3–6]. The continuous presence of those and other pharmaceutical compounds causes continuous poisoning on aquatic surfaces due to their toxicity and low biodegradability. In addition to being a potential threat to the health of humans and animals, the prolonged release of antibiotics can cause serious problems, including the development of microorganisms that resist antibiotics, a concern that has become notorious the world over [4,5,7,8].

Tetracyclines are the second-most consumed family of antibiotics globally due to their low cost, easy synthesis, and favorable antimicrobial activity based on the inhibition of protein synthesis [9–11]. Although primarily used to treat bacterial infections of the skin, intestines, respiratory tract, urinary tract, genitals, lymph nodes, and other body systems, tetracyclines are also used to treat severe acne and

* Corresponding authors.
E-mail addresses: e.gomez@ub.edu (E. Gómez), r_dhahri@yahoo.fr (R. Dhahri), a.serra@ub.edu (A. Serrà).

https://doi.org/10.1016/j.cej.2021.132006
Received 15 June 2021; Received in revised form 17 August 2021; Accepted 20 August 2021
Available online 27 August 2021

sexually transmitted diseases such as syphilis, gonorrhea, and chlamydia. Beyond that, they are additionally used in veterinary medicine and agriculture to aid the growth of animals. As such, tetracycline (TC) has been identified as the most widely used tetracycline antibiotic in the livestock industries of many countries, including the United States, China, and India, owing to their low cost and extensive production [3,6,9,11]. The continuous release of TC-based antibiotics in the world's waters poses a risk to human health, however, as bacteria become resistant and the antibiotics consequently become ineffective in preventing, controlling, treating, and spreading infectious diseases [3,9,12].

Although several methods of water purification and disinfection are useful—chlorination, ozonation, hydroperoxidation, and UV radiation, among others—they can be costly, especially for underdeveloped communities. Safer, less expensive methods are therefore needed, especially for parts of the world that cannot afford costly water treatment. Apart from that, conventional wastewater treatment plants cannot eliminate TC-based antibiotics due to their low biodegradability, and alternative treatments have therefore been actively sought for years [1–3,13]. As a potential solution, advanced oxidation processes (AOP) represent the most efficient technology for mineralizing persistent, resistant, and non-degradable organic pollutants in aquatic environments. For that reason, AOPs have played an important role in the treatment of water and wastewater in recent decades [2,14].

Among the different AOPs, sonocatalysis and, more prominently, photocatalysis have emerged as two of the most promising techniques for decontaminating water. On the one hand, in sonocatalysis, once ultrasound vibrations are generated, ultrasonic waves in the liquid environment produce acoustic cavitation, which consequently forms vast amounts of microscopic bubbles in the water [15–18]. Containing an abundance of energy, the bubbles eventually collide, which breaks the chemical bonds and induces the formation of hydroxyl radicals, which are responsible for the photooxidation of organic pollutants. Ultrasound vibrations continuously clean the surface of the catalysts and improve the mass transfer between the surface and the solution reaction [15,19]. On the other hand, photocatalysis is based on the absorption of photons with an energy equal to or greater than the energy bandgap, which causes the photoexcitation of electrons (e^-_{CB}) from the filled valence band (VB) to the empty conduction band (CB) in a process that generates holes (h^+_{VB}). As a consequence, h^+_{VB}, as strong oxidants, can directly oxidize organic pollutants and react with water, thereby promoting the formation of hydroxyl radicals—the second-strongest oxidant known—whereas e^-_{CB}, as reducing species, react with dissolved oxygen to generate superoxide radicals, oxygen peroxide, and even more hydroxyl radicals [2,20–23]. In this context, ZnO and ZnO-based catalysts have been in the spotlight of research for sono- and photocatalysis in different disciplines. Doping ZnO with metal ions is one of the most promising strategy to modify both electronic and optical performance as well as hinder the high photocorrosion of ZnO. Although alkali and alkaline earth metals have excellent solubility and good electrical and thermal conductivity they have been rarely investigated as ZnO dopants in sono- and photocatalytic water decontamination process [24–26]. Among those metals, DFT studies confirmed that Ca doping pose excellent ability to modulate the optical properties and photocatalytic performance of ZnO [24,27]. The optical band gap of Ca doped ZnO can be shifted toward red. The incorporation of Ca can enhance the optical absorption toward the visible light range and serves to control the recombination of the excitations. In addition, due to the substitution of the Zn^{2+} site for the Ca^{2+} site, additional support could be produced such as oxygen deficiencies, interstitials, among others, which can be positive for sono- and photocatalytic purposes [24–26].

On top of that, a recent exploration of the synergetic combination of both processes resulted in a joint process called *sono-photocatalysis*. In sono-photocatalysis, a semiconductor is irradiated while acoustic waves are created in the medium, which facilitates the generation of different free radicals (Scheme 1) and consequently the higher photooxidation of organic pollutants [17,18]. Several proposals concerning the synergistic effect of light and ultrasound suggest an increased concentration of free radicals due to photocatalytic and sonocatalytic effect on hydrogen peroxide [17,18,28]. Researchers have attributed that synergistic effect to lower bandgap produced by high temperatures and/or high pressure due to ultrasound waves, along with the corresponding effect on photocatalysis. The formation of an internal electric field also seems to promote the separation of charge carriers and consequently reduce recombination losses. Moreover, ultrasonic collapse improves mass transfer between the surface of the catalyst and the liquid phase, while the acoustic wave increases the dispersion of the catalyst, keeps its homogeneous throughout the solution, and cleans impurities from its surface [17,18,28,29]. However, despite the improvement in catalytic activity as a consequence of the synergistic effects, few studies have evaluated the stability and, more specifically, the sono-photocorrosion of the catalysts. Nevertheless, those features are critical for the development of the new technology for water decontamination.

Herein, the 30-day chemical stability of TCs as well as the adsorption and sonocatalytic, photocatalytic, and sono-photocatalytic mineralization of TC on ZnO and Ca-doped ZnO nanoparticles at different pH have been reported. The significantly improved mineralization of TC was observed, independently on both the pH and catalyst, when light and ultrasound were simultaneously applied. The reusability of catalysts was also investigated, and a mineralization mechanism was proposed. To demonstrate the potential of the sono-photocatalytic process using new ZnO-based photocatalysts, the sonocorrosion, photocorrosion, and sono-photocorrosion of ZnO and Ca-doped ZnO nanoparticles were systematically evaluated. Contrary to expectations, sono-photocatalysis did not result in the greater dissolution of the catalyst, which was the same or slightly less (i.e., between 10% and 28% of the catalyst dissolved after 24 h) than that observed for photocorrosion. That finding supports the use of sono-photocatalysis.

2. Experimental

2.1. Synthesis and characterization of Ca-doped ZnO nanoparticles

Scheme S1 shows the protocol of pure and Ca-doped ZnO nanoparticles prepared using the sol–gel technique. At first, 16 g of zinc acetate ($Zn(CH_3COO)_2{\cdot}2H_2O$, 99%) were dissolved in 112 mL of methyl alcohol. The mixture was magnetically stirred for 10 min at ambient temperature. Then a satisfactory amount of calcium chloride hexahydrate ($CaCl_2{\cdot}6H_2O$) with different [Ca]/[Zn] proportions of 0, 0.01, 0.02 and 0.03 were added to acquire Ca-doped ZnO nanoparticles. After stirring for 15 min, the obtained solution was put in an autoclave and dried in the supercritical states of ethanol (Tc = 243 °C; Pc = 63.6 bar). Every one of the synthesized samples was then warmed in a heater for two hours at 400 °C in air. The names of the samples are C0ZO, C1ZO, C2ZO and C3ZO, depending on the nominal load of Ca in each sample.

To study the different properties of the obtained samples, several characterizations were made. The microstructure of the samples was shown from XRD patterns using a Bruker D8 Advance A 25 X-ray diffractometer with a CuK_α radiation source (1.54 Å) operating at 40 kV. To get information about the morphology of the nanopowders Scanning Electron Microscopy (SEM) was performed at 15 kV with a ZEISS 154XB FE SEM instruments; also by carrying out Transmission Electron Microcopy (TEM) utilizing a JEOL 2010 EX instrument operating at 200 kV. EDX elemental mappings of ZnO-based nanopowders were performed using a FEI Magellan 400 L XHRSEM equipped with an Oxford Instruments Ultim Extreme EDX detector system. The spectrum 100 Perkin-Elmer FTIR spectrophotometer was used to do Fourier Transform Infrared Spectroscopy (FTIR). The chemical states of the surface of each catalyst were investigated using X-ray photoelectron spectroscopy (XPS) with a SPECS PHOIBOS 150 hemispherical analyzer using monochromatic Al Kalpha radiation (1486.74 eV) as the excitation source.

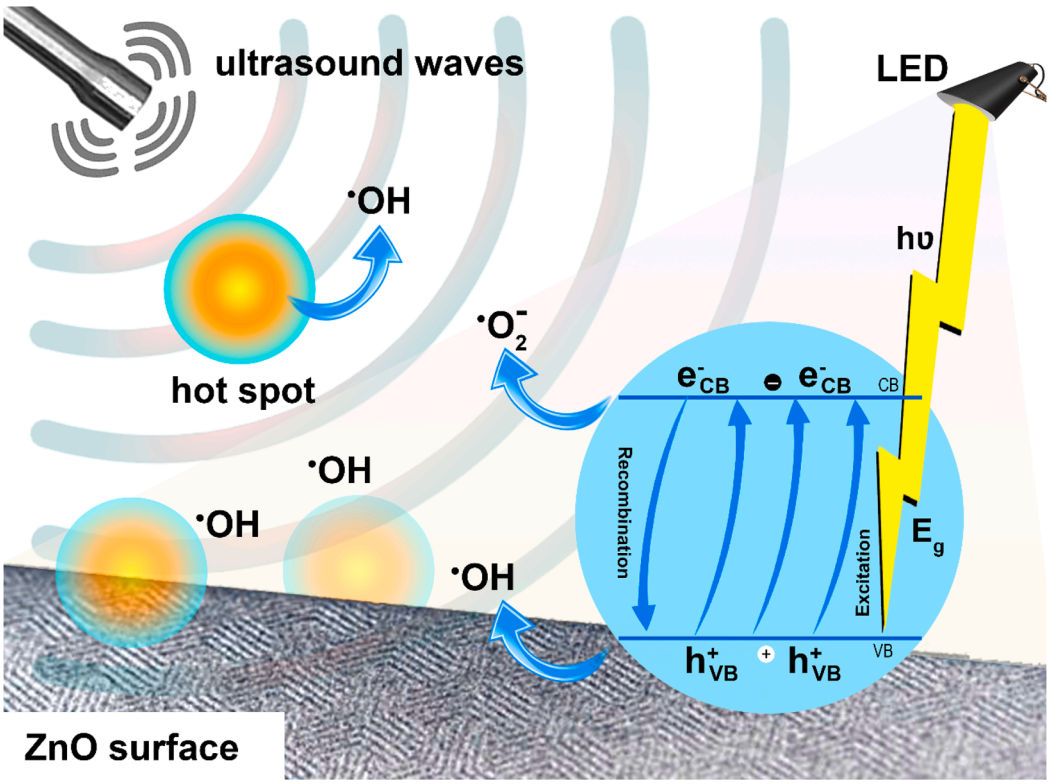

Scheme 1. Schematic representation of sono-photocatalytic process.

Inductively coupled plasma (ICP) analysis was carried out for each catalyst on an inductively coupled plasma atomic emission spectroscopy (Perkin-Elmer Optima 5300 dual). To show the optical properties and study the defects located at the nanomaterials bandgap, one has performed PL measurements by the NanoLog Horiba modular spectrofluorometer. The Xe lamp is the excitation light source at room temperature. An excitation wavelength of 325 nm was applied and the emission between 350 and 750 nm was recorded. The UV–vis Diffuse Reflectance Spectra (DRS) were obtained with a UV–vis spectrophotometer (PerkinElmer, Lambda 900 UV). The photocurrent experiments were carried out with a PGSTAT30 potentiostat–galvanostat Autolab and the NOVA software using a three-electrode system. Pt wire was used as the counter electrode, Ag/AgCl/KCl (3 M) electrode as a reference and the prepared photocatalysts as working electrodes. The working electrodes were prepared by dropping 100 μL of each CZO catalyst suspension on the surface of FTO electrode and then dried under nitrogen air before the electrochemical experiments to form an homogeneous catalyst coating. The electrolyte used for all those experiments was a 0.5 M Na_2SO_4 (pH = 7.0) solution. The chronoamperometry test was recorded at 0.6 V versus the Ag/AgCl/KCl (3 M) electrode under LED light in 30-s on–off cycles. The charge transfer of CZO catalysts was investigated via electrochemical impedance spectroscopy (EIS) measurements, which were performed at the open circuit potential at frequencies range from 100 kHz to 10 MHz with AC amplitudes of ±5 mV.

2.2. Stability and adsorption of tetracycline

The chemical stability of TC, in the absence of light, was investigated for 30 days. The effect of pH on chemical stability was also investigated. For this purpose, 150 mL of single-pollutant TC (10 ppm) solutions were maintained at 20 °C in dark conditions in stagnant conditions. The temporal evolution of the UV–vis spectra (200 to 500 nm) was monitored by a UV–vis spectrophotometer (Shimadzu UV-1800). In addition, the Total Organic Carbon (TOC) content in the single-pollutant solutions was measured by the high-temperature combustion method using TOC-VCSH equipment (Shimadzu) with a high-sensibility column. All the experiments were performed in triplicate.

Adsorption experiments were performed to determine the adsorption–desorption equilibrium time of TC on ZnO-based photocatalysts at 20 °C in dark conditions. The effect of pH (i.e., 4,6,8, and 10) on the adsorption–desorption process was also investigated. Typically, 25 mg of the photocatalyst was suspended in 50 mL of a single-pollutant solution (10 ppm of TC) and maintained under magnetic stirring (400 rpm) and in the absence of light. After a certain time, during 120 min, 1 mL of the suspension was fetched, centrifugated and filtered through a 0.22 μm syringe filter to determine the TC concentration. The TC concentration was measured by UV–vis spectrophotometer (Shimadzu UV-1800). Measurements were carried out in the range of 200–500 nm to determine this maximum wavelength peak and its correspondent absorbance. All the experiments were performed in triplicate.

2.3. Mineralization of tetracycline

The mineralization experiments were performed at pH 6 and 8 to evaluate the photolytic, sonolytic, and sonophotolytic degradation of TC in independent experiments were performed. In a typical manner, 150 mL of TC solution (10 ppm) was illuminated with a 1.6 W white LED strip (2.2×10^{-3} W cm^{-2}) or/and sonicated with a frequency of 40 kHz and 100 W output power for 180 min. Fig. S1 depicts the normalized irradiance spectrum of the white LED strip. Both experiments were done by triplicate in the dark, to determine that the degradation process was exclusively the action of LED's or ultrasounds. The temperature of the reaction medium has been controlled by circulating cold water during the irradiation processes, thus maintaining the temperature at approximately 20 °C. Aliquots of 0.5 mL were extracted every certain time range, from 0 to 180 min. These were put in the refrigerator immediately after extraction and, the effective mineralization was determined by measuring the reduction in the TOC content.

Next, the sonolytic, photocatalytic and sono-photocatalytic degradation of TC were investigated. Table 1 summarizes the experimental

Table 1
Experimental conditions for sonocatalytic, photocatalytic, and sono-photocatalytic evaluation.

Experiment	Volume/ mL	TC/ ppm	Cat/mg mL^{-1}	Magnetic stirring/ rpm	Temperature/ °C	Light irradiation	US irradiation	Time/ min
Sonocatalysis	150	10	0.5	400	20.0	–	40 kHz and 100 W	180
Photocatalysis	150	10	0.5	400	20.0	1.6 W white LED (2.2×10^{-3} W cm^{-2})	–	180
Sono-photocatalysis	150	10	0.5	400	20.0	1.6 W white LED (2.2×10^{-3} W cm^{-2})	40 kHz and 100 W	180

conditions for the sonocatalytic, photocatalytic, and sono-photocatalytic evaluation.

At a certain time, 1 mL of the suspension was fetched, centrifugated and filtered through a 0.22 μm syringe filter to determine the TOC content. In addition, the major intermediate products formed during the degradation process were determined by liquid chromatography-mass spectroscopy (LC-MS, Waters Xevo G2-XS QToF) analysis [3]. All the experiments were performed in triplicate. Next, the reusability of Ca-doped ZnO nanoparticles was also investigated by measuring the mineralization of 10 ppm fresh solutions for 10 consecutive cycles for sonocatalytic, photocatalytic and sono-photocatalytic experiments.

Trapping experiments were performed to determine the role of reactive oxygen species on the degradation process of TC. Isopropyl alcohol (quencher of hydroxyl radicals), benzoquinone (quencher of superoxide radicals), and triethanolamine (quencher of photogenerated holes) were used for this purpose. In a typical experiment, the single-pollutant solution containing the radical scavenger (1 mM of scavenger) was irradiated for 180 min using a 1.6 W white LED strip (2.2×10^{-3} W cm^{-2}) or/and sonicated with a frequency of 40 kHz and 100 W output power. Next, the TOC was measured using. All experiments were

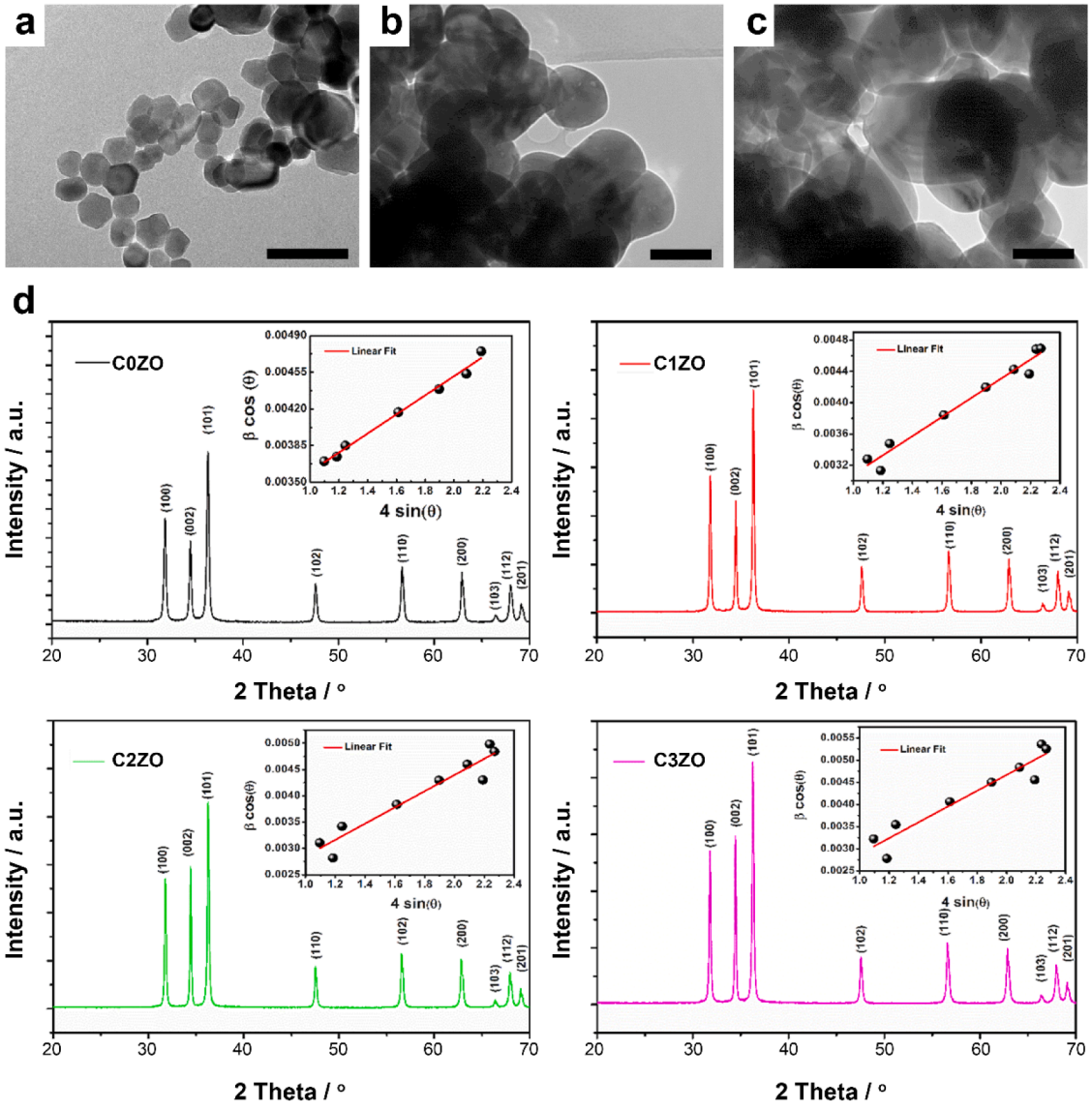

Fig. 1. TEM micrographs of (a) C0ZO, (b) C1ZO, and (c) C3ZO nanoparticles and (d) X-ray diffraction patterns of the CZO samples with Williamson–Hall plots (inset). Scale bar: 100 nm.

performed in triplicate. To further investigate the role of hydroxyl and superoxide radical's electron paramagnetic resonance (EPR) measurements in in 5,5-dimethyl-1-pyrroline-N-oxide (DMPO) were carried out with a Bruker A200-9.5/12 spectrometer in the dark and under LED irradiation.

2.4. Chemical, sonochemical, photochemical and sonophotochemical stability of Ca-doped ZnO nanoparticles

ZnO NPs can dissolve and release Zn(II) ions when subjected to light and ultrasound irradiation. The effect of visible light and ultrasound irradiation, if not both, on the ZnO stability was investigated. In a typical experiment, 150 mL of Milli-Q water, containing 75 mg of each photocatalyst, were subjected to (i) 48 h of continuously visible light irradiation, provided by a 1.6 W white LED strip (2.2×10^{-3} W cm^{-2}); or (ii) 24 h of ultrasound irradiation with a frequency of 40 kHz and 100 W output power. Note that in the sonocorrosion experiments, various short cycles have been performed (total time = 24 h) to avoid a significant increase in temperature. In addition, Milli-Q water has also been added to maintain the same final volume. The effect of pH on the photocorrosion and sonocorrosion processes was also investigated. At a certain time, 1 mL of the suspension was fetched, centrifugated and filtered through a 0.22 μm syringe filter to determine the Zn(II) concentration. The Zn(II) concentration was spectroscopically quantified by UV–vis spectrophotometer (Shimadzu UV-1800) using Zincon reagent [30]. All the experiments were performed in triplicate.

3. Results and discussion

3.1. Synthesis and characterization of Ca-doped ZnO nanoparticles

Fig. 1 presents TEM images showcasing the morphology of pure and Ca-doped ZnO nanopowders heat-treated at 400 °C for 2 h. The ZnO nanopowders were composed of an agglomeration of uniform spherical grains, as exemplified in Fig. 1a. The shape of the crystallites was prismatic with a narrow distribution of particle sizes, mostly between 20 and 50 nm. By adding Ca, larger and agglomerated particles could be observed on doped samples, as illustrated in Fig. 1b and c. The elemental mapping images (Fig. S2) shows that the distribution of Ca is less dense, although it increases when increasing the doping percentage, than those of Zn and O. Importantly, the distribution of Ca, Zn and O were similar which indicate the coherent distribution and incorporation of Ca in the ZnO matrix.

Typical X-ray diffraction patterns of pure and Ca-doped ZnO nanoparticles heat-treated at 400 °C for 2 h in air appear in Fig. 1d. In all samples, only the reflection peaks of hexagonal wurtzite polycrystalline ZnO material emerged, namely along the (100), (002), (101), (102), (110), (200), (103), (112), and (201) planes according to the JCPDS database (Card No. 36-1451) [31]. The lack of obvious peaks due to other phases (e.g., CaO) in the spectra suggests the high purity of the prepared samples. Similar results were obtained by Kulkarni et al and Umavathi et al. [32,33], as well as by Irshad et al., who suggested that CaO's absence stemmed from the fact that Ca ions are incorporated in the ZnO network or may exist in an amorphous form [34]. A slight shift of the XRD peaks toward lower 2-theta degrees was observed as the concentration of Ca increased, as detailed in Table 2. That trend, likely resulting from the difference in radii of Ca (r = 197 pm) and Zn (r = 134 pm), indicates a local distortion of the ZnO lattice due to residual stress in the nanoparticles.

Table 2
Geometric parameters of different samples, with estimated D values.

	a (Å)	c (Å)	V (Å^3)	D_{W-H} (nm)	ε	2 θ $_{(101)}$	δ (10^{-4} line × nm^{-2})
C0ZO	3.244	5.195	47.338	51	0.0009	36.3164	8.15
C1ZO	3.251	5.2	47.594	77	0.0012	36.2917	7.19
C2ZO	3.257	5.201	47.779	106	0.0015	36.2508	6.52
C3ZO	3.261	5.203	47.915	126	0.0018	36.2501	6.57

The Williamson–Hall method was used to determine the average crystallite size and the lattice strain of an imperfect crystal [35-37]. The plots of $\beta cos\theta$ as a function of $4sin\theta$ appear in the inset of Fig. 1, with the slope of the fit line indicating the value of the lattice strain and the y-intercept indicating the crystallite size. In addition, Table 2 shows that the average crystallite size seems to have increased with incrementally greater dopant loads: 51 nm for pure ZnO and 126 nm for C3ZO.

The FTIR spectra of pure and Ca-doped ZnO nanoparticles are presented in Fig. 2a. The same broadband in all spectra, located at 3,481–3,460 cm^{-1}, corresponded to O–H stretching. By contrast, the absorption band detected at 1,640–1,632 cm^{-1} corresponded to the bending vibrations of water molecules [38,39]. A new band, appearing at 1,420 cm^{-1} once Ca was added, was attributed to the formation of carbonate species [40]. Otherwise, the band at 843–835 cm^{-1} corresponded to C–H bending, and the band at 691–530 cm^{-1} was attributed to M-O-M (M = Zn, Ca) [41,42].

XPS analysis was performed to analyze the elemental chemical states and to confirm the Ca presence and incorporation of Ca during the sol–gel process. The binding energies obtained from the XPS analysis were corrected for specimen charging by referencing the C 1s to 284.60 eV. The relative amount of Ca on the surface of each doped catalyst varies from 1.03%, 2.08%, and 3.11% for C1ZO, C2ZO, and C3ZO, respectively. Those percentages were practically identical to those obtained by ICP analysis (1.07%, 2.13% and 3.06% for C1ZO, C2ZO, and C3ZO, respectively), confirming that Ca was homogeneously distributed throughout the entire structure. As shown in Fig. 2b, the Zn $2p_{1/2}$ and Zn $2p_{3/2}$ core levels of C0ZO were centered at 1044.9 eV and 1021.8 eV, respectively, being the split spin–orbit components 23.1 eV, which is consistent with other ZnO architectures [43,44]. C1ZO, C2ZO, and C3ZO also presented the same peaks, but centered at slightly lower binding energies, being smaller the higher Ca doping, due to the incorporation of Ca into the ZnO lattice. This behavior has been reported previously for other Ca-doped ZnO materials [45]. This shifting to slightly lower binding energies can be explained by the lower electronegativity of Ca incorporated into the ZnO lattice, causing an electron screening effect on Zn [45,46]. Fig. 2c shows the Ca 2p core level of CZO catalysts, with to peaks centered at approximately 350.4 eV and 346.9 eV, corresponding to the Ca $2p_{1/2}$ and Ca $2p_{3/2}$ spin–orbit components, confirming the presence and incorporation of Ca ions in the ZnO lattice. Note that the same profile was observed after several argon ion sputtering cycles, indicating the consistence of distribution throughout the entire structure.

The UV–vis DRS spectra of pure and Ca-doped ZnO nanoparticles (Fig. 3a) were recorded to evaluate the absorption behavior and the possibility of using visible light for photocatalytic water decontamination. As expected, the non-doped ZnO nanoparticles exhibited an absorption peak at approximately 375 nm (i.e., in the UV domain), whereas the Ca-doped ZnO nanoparticles showed an absorption tail in the range of 400–500 nm, in which the absorption intensity is the maximum for 2 at % of Ca doping. Such a redshift in the photosensitivity of Ca-doped ZnO likely derived from the sub-bandgap transitions generated by the incorporation of Ca ions in ZnO's structure. Note that at the highest doping of ZnO by Ca, the 400 nm absorption tail does not continue to increase compared with C1ZO and C2ZO but decreases. This fact is possibly attributed to the presence of CaO, which it has a high absorption value at the 400 nm absorption tail.

The PL spectra of undoped and Ca-doped ZnO nanoparticles appear in Fig. 3b. The PL spectra of the nanostructures of CZO nanopowders derived from an NBE emission in the UV region and a broad peak in visible light due to a deep-level emission (DLE). The NBE peak shifted to shorter wavelengths with Ca doping, which may relate to the Moss Burstein effect. The replacement of Zn^{2+} ions, present in their network sites, by the substitution of Ca^{2+} ions in the CZO nanostructures

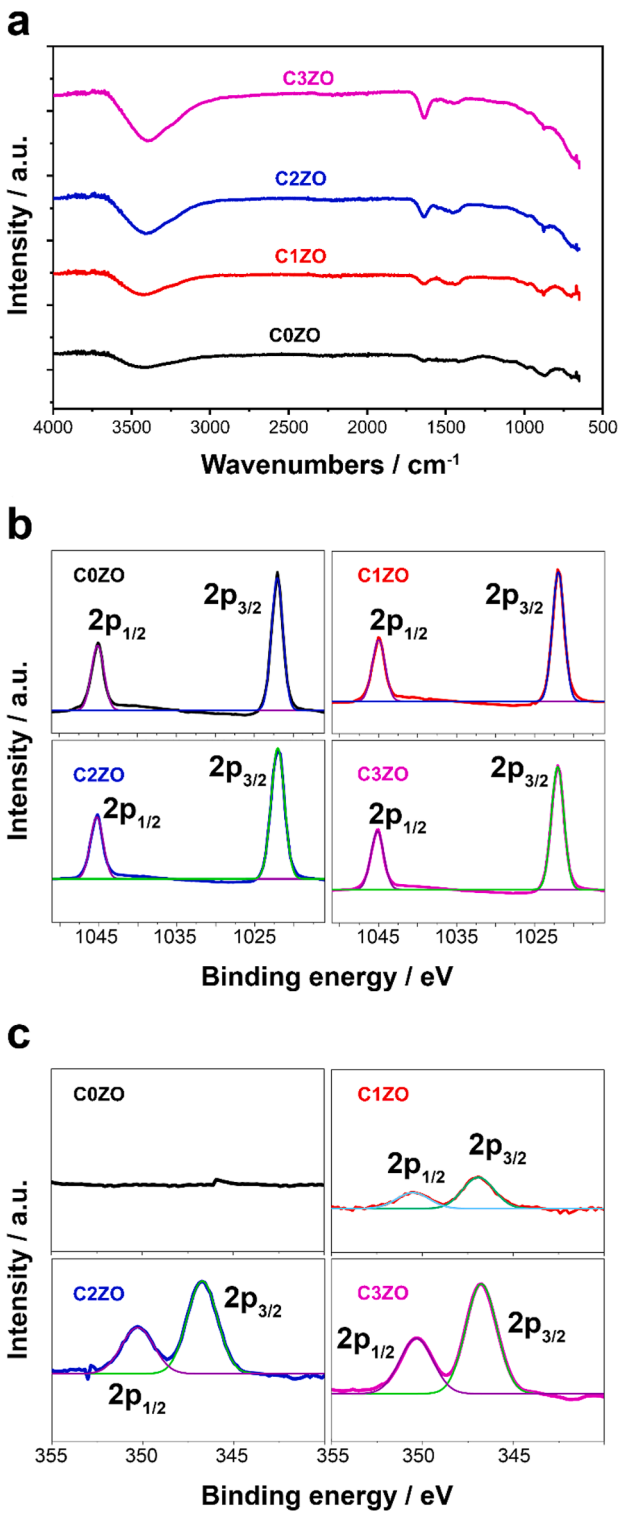

Fig. 2. (a) FTIR and XPS spectra of (b) Zn 2p and (c) Ca 2p of the different CZO nanoparticles.

generally raises the Fermi level and widens the optical band gap. The energy deviation values calculated with the Tauc formula from UV–vis DRS confirm the maximum blue offset of the NBE. The increase in peak intensity in both DLE and NBE regions, as a function of an increased rate of Ca doping, indicates that defects in ZnO's structure increased as well, because Ca-doped ZnO photocatalysts should be more active under visible light irradiation. Doping by Ca causes a rapid increase in the intensity of emission such that the intensity is proportional to the increase in the percentage of doping. This is attributed, primarily, to the replacement of Zn^{2+} ions which have a smaller atomic radius (0.88 Å) by Ca^{2+} ions which have a stronger atomic radius (1.14 Å) compared with that of zinc ions. This replacement serves to disrupt the sites in the crystal structure and increase the content of defects in the material. As a result, an increase in the rate of oxygen deficiency (V_o) has been obtained, attributed to green emissions and in the rate of interstitial zinc (Zn_i) attributed to red emissions[41,47].

To confirm the photoexcited charge generation of the CZO catalysts under visible LED irradiation photocurrent experiments were carried out. Fig. 3c shows the j-t transients at 0.6 V versus Ag/AgCl/ KCl (3 M) under visible light 30s on–off cycles. The data evidenced residual currents in dark for all the catalysts, but under visible LED irradiation, the photocurrents increased sharply, which indicates generation and separation of photoexcited electron-hole pairs. This behavior was consistent with the EIS Nyquist plots (Fig. 3d). Under visible light irradiation, the effect of Ca doping in lowering the bandgap and facilitate the generation of electron-hole pairs was clear as C1ZO, C2ZO and C3ZO exhibit photocurrent 3.5, 7.8, and 5.8 times higher than the non-doped ZnO nanopowder. The high photoelectrochemical response and its stability during time indicate that the presence of 2 at. % of Ca into the ZnO lattice significantly improves the charge transfer and minimizes the charge carrier recombination. To further investigate the effect of Ca doping on the charge transfer resistance and separation efficiency of photogenerated electrons and holes EIS measurements were performed. Fig. 3d shows the EIS Nyquist plots for CZO under visible LED irradiation. The C2ZO arc radii was significantly smaller than the non-doped nanopowder, which indicates less electrochemical resistance and consequently improved the transfer of photogenerated charge carriers across the solid–liquid junction. The electrochemical resistance followed the same trend than photocurrent experiments: C2ZO < C3ZO < C1ZO < C0ZO. This fact confirms that Ca doping, and more especially 2 at% of Ca doping, promotes the separation efficiency of photogenerated electron-hole air and faster the charge transportation in the interface, which is pivotal for photocatalytic applications.

3.2. Stability of TC

3.2.1. Chemical stability of TC as a function of pH in dark conditions

The chemical stability of TC (Fig. S3) was studied over 30 days in the dark conditions at four different pH (i.e., 4, 6, 8 and 10). As shown in Fig. S3, at pH = 4 and pH = 6 the UV–vis spectra of TC were virtually constant throughout the 30-day period. The Fig. also illustrates how the absorbance slightly decreased during the period, which indicates the high stability of the species at moderate and slightly acidic pHs. At pH = 8, TC followed a fairly constant trend of degradation throughout the period as the absorbance continuously lessened. Although TC suffered from degradation at pH = 8, the degradation did not have high values, with a maximum absorbance reduction of less than 25%. The formation of other species could not be distinguished, however, because the UV–vis spectra presented the same profile. By contrast, at pH = 10, the spectra seemed somewhat constant in that they started to show overlapping peaks due to the formation of intermediates during the degradation process. Clearly, slightly and moderately alkaline pH levels favored the degradation of TC. Even so, the presence of TC and/or their derivatives in aquatic ecosystems such as rivers and reservoirs persists in the long term. Regardless of pH, however, TCs do not mineralize independently, because the TOC does not vary.

3.2.2. Photolysis, sonolysis and sonophotolysis of TC

The effect of light and/or ultrasound on the mineralization of TC was systematically investigated in the absence of any catalyst. As shown in Fig. 4, the sonolytic, photolytic, and sonophotolytic mineralization of TCs was affected by the solution's pH. In all cases, mineralization was more significant as pH increased. After 180 min of irradiation, mineralization values ranged from 9% (pH = 4) to 24% (pH = 10) for

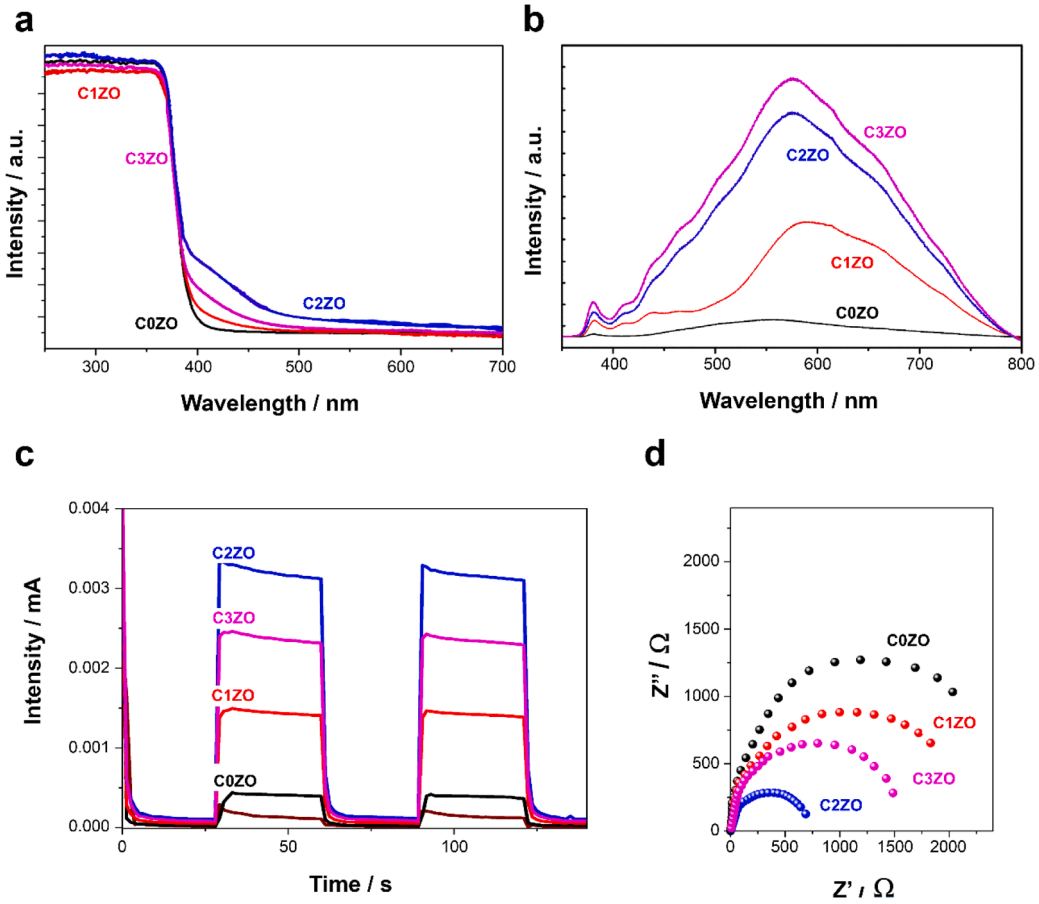

Fig. 3. (a) UV–vis DR, (b) PL spectra, (c) amperometric photocurrent curves measured at 0.6 V versus Ag/AgCl/ KCl (3 M) under visible light 30-s on–off cycles, and (d) the EIS Nyquist plots of the different CZO nanoparticles at room temperature.

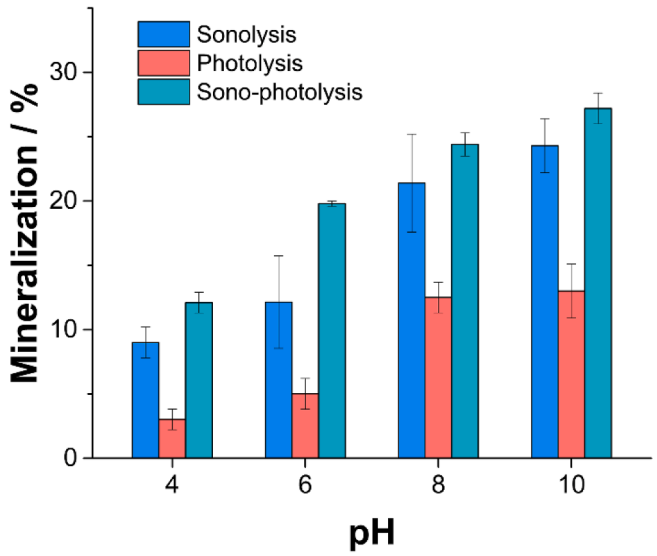

Fig. 4. Sonolytic, photolytic, and sonophotolytic mineralization of TC at 20 °C at different pH after 180 min of irradiation. Error bars indicate standard deviations of the three replicated experiments.

sonolysis, from 3% (pH = 4) to 13% (pH = 10) for photolysis, and from 12% (pH = 4) to 27% (pH = 10) for sono-photolysis. Moreover, as the pH increased, the amount of TC^- anion increased, which generally tends to promote the absorption of reactive oxygen species such as $^{\bullet}OH$ radicals. Those results suggest the need to use a catalyst, because the mineralization values were relatively low, and using a catalyst would efficiently improve the removal of the antibiotic.

3.3. Study of adsorption of TC on ZnO and Ca-doped ZnO nanoparticles

The level of pH also plays a fundamental role in the adsorption processes between TC and photocatalysts. TCs are amphoteric molecules that present as cationic species at pH less than 3.3, in a zwitterionic form in the pH range of 3.3–7.7, and as anionic species TC^- or TC^{2-} when pH exceeds 7.7 [48-50]. By contrast, the isoelectric point of undoped ZnO was 8.7, whereas those points of C1ZO, C2ZO, and C3ZO were 8.9, 9.0, and 9.2, respectively. Depending on the medium's pH, the speciation of TC and the catalyst's surface charge vary, which can either favor or hinder the TC adsorption on the catalyst's surface (Fig. S4) [2].

To gauge the effect of pH on the adsorption dynamics of TC, the adsorption capacities at different times (q_t) and in equilibrium (q_e) were spectroscopically identified [51]. As shown in Fig. 5, the difference in adsorption was remarkable depending on the medium's pH. The most suitable pH levels for adsorption were pH = 6 and pH = 8, and the catalyst that exhibited a higher adsorption capacity was the one doped with 2 at. % Ca (Table 3). At pH = 6, the primary TC species was the zwitterionic form even though the photocatalyst's surface was primarily positive. In those conditions, the electrostatic interaction did not negatively affect adsorption. However, at pH = 8, the negatively charged TC^- was the dominant pollutant species, whereas the surface charge density of the photocatalyst was positive. Consequently, electrostatic interaction between both entities favored their general interaction. At pH = 4, however, the photocatalyst's surface charge density was positive, and

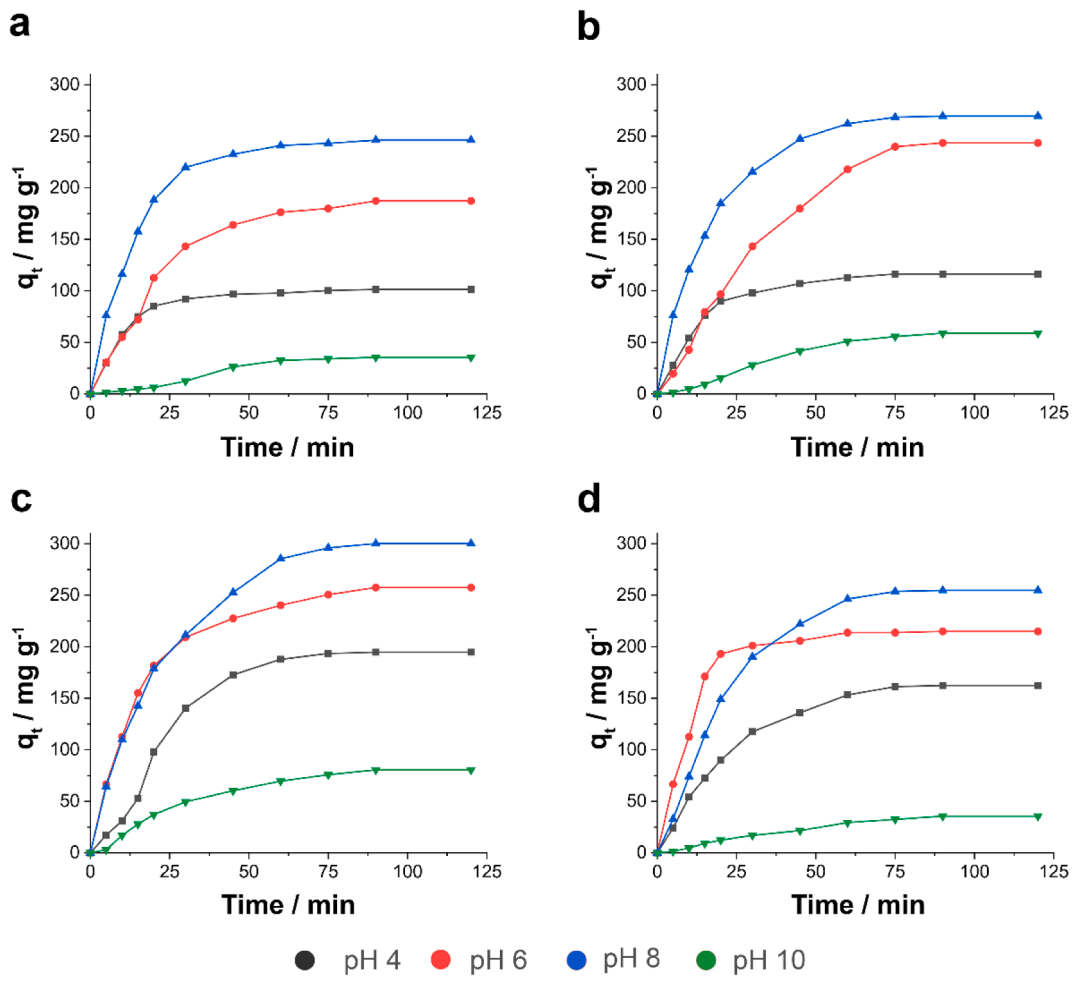

Fig. 5. Variation in the adsorption of TC on the catalyst's surface at certain times for (a) C0ZO, (b) C1ZO, (c) C2ZO, and (d) C3ZO at 20 °C.

Table 3
Adsorption capacity in the equilibrium of TC on ZnO-based nanoparticles as a function of the pH value.

pH	q_e/mg g^{-1}			
	C0ZO	C1ZO	C2ZO	C3ZO
4	101.4	116.4	194.7	162.4
6	187.3	214.9	257.5	243.6
8	246.3	269.6	300.2	254.8
10	35.6	58.8	80.5	35.6

the primary TCs were in zwitterionic form, even though a considerable percentage (approx. 20%) were in the positive form as well. That behavior translated into a reduction in adsorption capacity in the equilibrium compared with pH = 6 when TC were entirely in their zwitterionic form. Last, at pH = 10, the catalyst's surface and TC molecules had the same sign, which translated into a significantly lower adsorption capacity at equilibrium. On the whole, the adsorption process can be mainly explained by the electrostatic interaction between the charges of TCs species and the catalyst.

Comparing the different photocatalysts benefits from considering each material's effective BET surface area, which for C0ZO, C1ZO, C2ZO, and C3ZO were 11.6, 12.4, 14.1, and 13.2 m^2 g^{-1}, respectively. The values of adsorption capacity at equilibrium rose as the effective area of the photocatalysts expanded, with the maximum achieved using the catalyst doped with 2 at. % Ca. However, the amount of TC adsorbed in relation to the effective area gradually rose for C1ZO but decreased as Ca content increased.

3.4. Catalytic performance of ZnO and Ca-doped ZnO nanoparticles in mineralizing TC

Based on the adsorption experiments and the approximate pH of most waters liable to contain TC or their derivatives, subsequent catalytic experiments focused exclusively on pH = 6 (Fig. 6) and pH = 8 (Fig. 7). As shown in Figs. 6 and 7, the differences between the catalysts were remarkable. For both levels of pH, the mineralization values increased (Table 4) in parallel to Ca doping except for 3 at. %, which reduced mineralization relative to 2 at %. The graphs in the figures show that although photocatalysis was more effective than sonocatalysis, combining them further improved mineralization. Meanwhile, sonocatalysis with all catalysts after 180 min of ultrasound irradiation hardly altered mineralization (approx. 55–57% and 57–58% at pH = 6 and pH = 8, respectively). The catalyst showing the best results was 2 at. % Ca, which reached mineralization values of 94.3% (pH = 6) and 94.4% (pH = 8) with photocatalysis and 99.8% (pH = 6) and 99.8% (pH = 8) with sono-photocatalysis. Moreover, after 90 min of irradiation, the sono-photocatalytic experiments achieved a mineralization value of nearly 100%. The highly improved mineralization of sono-photocatalysis was caused by synergetic effects between light and ultrasound waves, the latter of which can improve the mass transfer between the catalyst's surface and the liquid phase. On top of that, the morphology and composition of the semiconductor nanoparticles were not affected, and the synergistic effect may have stemmed from the disaggregation of particles induced by ultrasound, which facilitated light penetration and the cleaning of impurities from the catalyst's surface.

Regarding the effect of pH, at pH = 8 mineralization improved

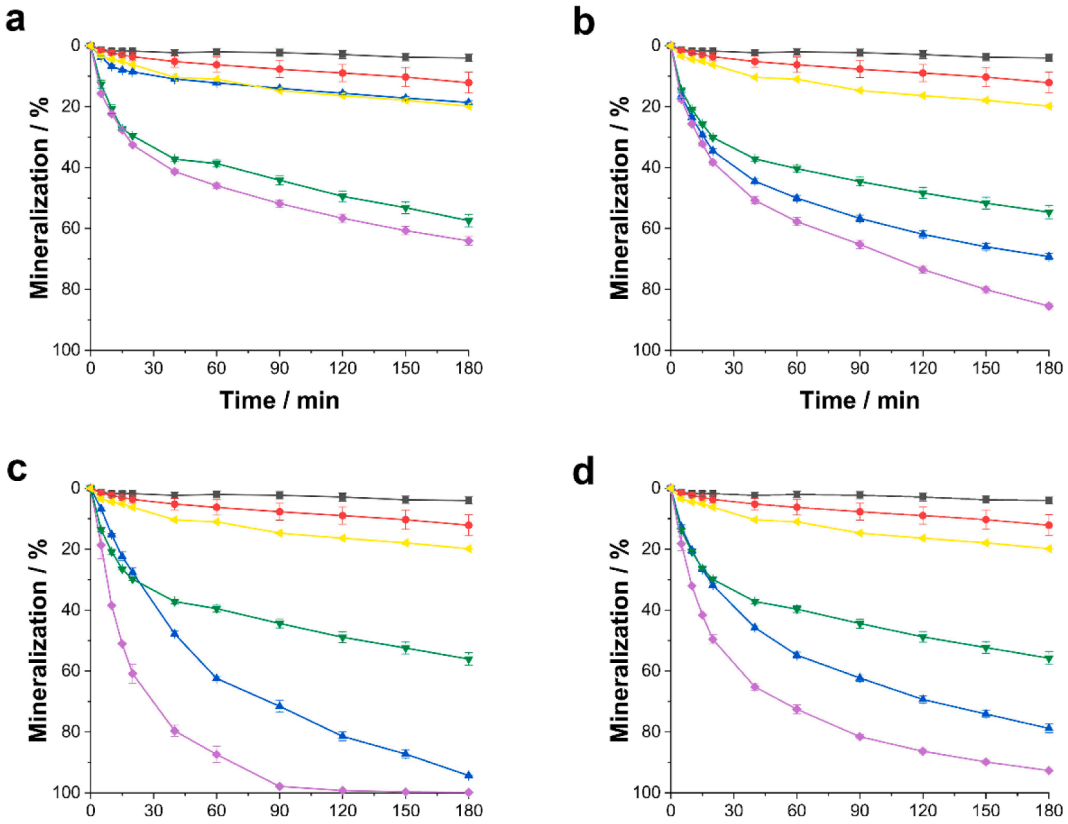

Fig. 6. Mineralization of TC using (a) C0ZO, (b) C1ZO; (c) C2ZO; and (d) C3ZO catalysts at 20 °C at pH = 6 after 180 min of irradiation. Error bars indicate standard deviations of the three replicated experiments.

compared with pH = 6, and at pH = 8, the adsorption of TC molecules was high/highest at pH = 8 and consequently facilitated the oxidation of TC. Among other results, the formation of reactive oxygen species was promoted in a moderately alkaline medium.

Ca-doped ZnO nanopowders emerged as promising visible-light driven sono-photocatalysts for mineralizing TC and their derivatives. Despite the difficulty of making rigorous comparisons between the different catalysts studied today, the Ca-doped ZnO nanopowders presented mineralization values similar to the most competitive state-of-the-art systems (Table 5). Beyond that, those highly competitive mineralization values were achieved using visible LED irradiation as a light source, which implies a significant reduction in energy consumption compared with classical sources such as halogen, Xe, and Hg lamps. Using light from LEDs significantly reduced energy costs associated with (sono-)photocatalytic treatment, which, combined Ca-doped ZnO catalysts' excellent performance, make them an important alternative for facilitating the design of more economical (sono)photoreactors. Although apparent quantum yield is not the best way to evaluate the energy efficiency of the tetracycline mineralization by a sonophotocatalytic process, as it does not consider the effects of ultrasound, the average apparent quantum efficiencies ($\phi_{app,av}$), calculated on the basis of the mineralized TC molecules for a 90% conversion level, were calculated for C2ZO and C3ZO [52]. The $\phi_{app,av}$ values for the sono-photocatalytic process for C2ZO and C3ZO at pH = 6 and pH = 8 were ranged from 80% to 32% and 86% to 34%, respectively, which indicates excellent sonophotocatalytic performance to mineralize TC.

To clarify the role of the primary reactive species—hydroxyl radicals, superoxide radicals, and photogenerated holes—involved in degrading TC in the sonocatalytic, photocatalytic, and sono-photocatalytic processes, free radical trapping experiments were performed, using only C2ZO as the catalyst. As shown in Fig. 8a and b, in the case of sonocatalysis, regardless of the medium's pH, degradation is governed by hydroxyl radicals due to the negligible effect of scavengers of holes (h^+) and superoxide radicals ($^{\bullet}O^{2-}$). However, in photocatalysis and sono-photocatalysis at pH = 8, holes played a far more significant role, especially in photocatalysis. After 180 min of LED irradiation, degradation had fallen to 26%, 72%, and 4% in the presence of hole scavengers, superoxide radical scavengers, and hydroxyl radical scavengers, respectively. By contrast, after 180 min of LED and ultrasound irradiation, degradation had dropped to 46%, 87%, and 6% in their respective presence. Moreover, the same trend was observed at pH = 6. Those results demonstrate that degradation is primarily governed by hydroxyl radicals independent of the use of light and/or ultrasound irradiation, a circumstance that determines the kinetics and mechanism of the mineralization of TC. In addition, in order to probe the predominant effect of hydroxyl radicals the nature of the photogenerated reactive oxygen species under visible LED irradiation has been investigated via the EPR spectra of the DMPO-trapped $^{\bullet}OH$ in aqueous medium (Fig. 8c) and DMPO-trapped $^{\bullet}O^{2-}$ in methanol medium (Fig. 8d). As shown in Fig. 8c, the characteristic signal of DMPO-$^{\bullet}OH$ adduct was identified, indicating that the holes can be effectively transformed into $^{\bullet}OH$ radicals during the irradiation process. On the other hand, as shown in Fig. 8d, the characteristic signal of DMPO-$^{\bullet}O^{2-}$ adduct was also detected, which confirmed the formation of $^{\bullet}O^{2-}$. However, the peak intensity is significantly low compared with the DMPO-$^{\bullet}OH$. This result is consistent with the observed negligible role of $^{\bullet}O^{2-}$ during the mineralization process of TC using C2ZO catalyst.

To further investigate the sono-photocatalytic mineralization of TC, LC-MS was used to identify the major intermediates generated during irradiation at pH = 8. Samples extracted at different reaction times were analyzed, although the intensity of TC peaks (m/z = 445) decreased gradually during irradiation, non-negligible new peaks were detected during the total mineralization at m/z = 457, 414, 402, 365, 321, 312, 277, 214, 139, 91, 73, and 75 (Table S1). Based on those peaks, a

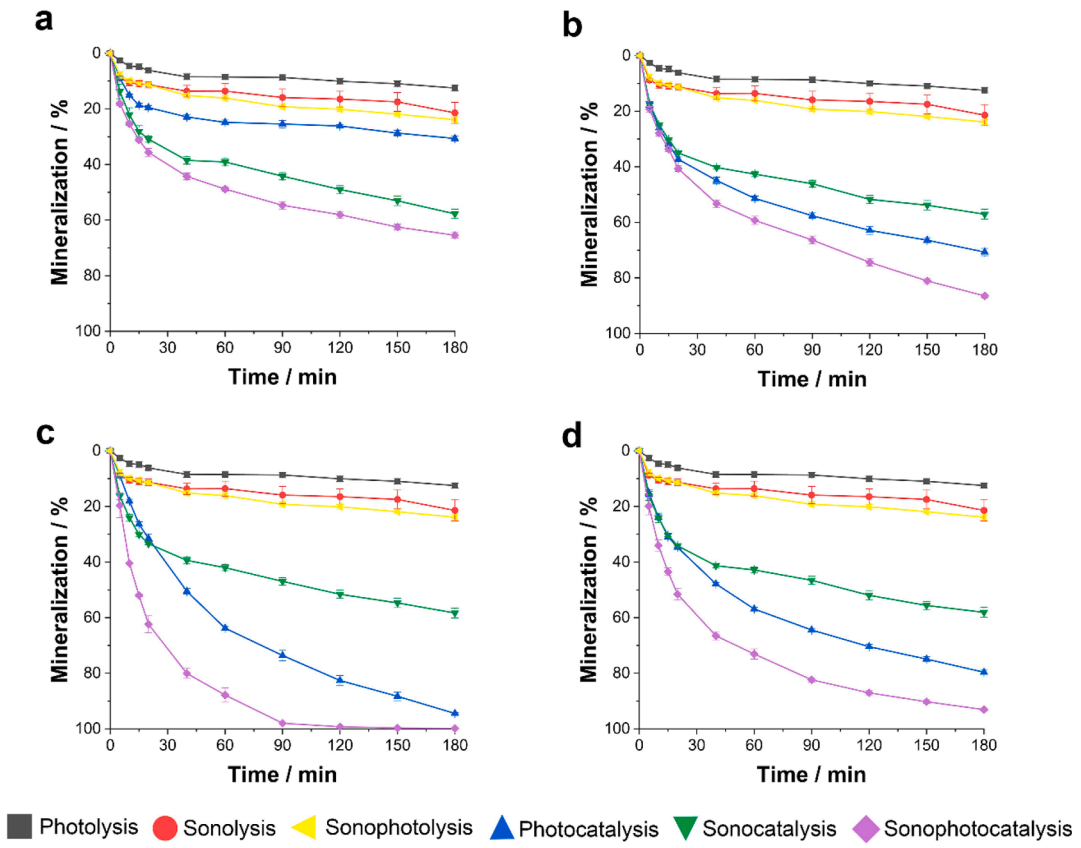

Fig. 7. Mineralization of TC using (a) C0ZO, (b) C1ZO, (c) C2ZO, and (d) C3ZO catalysts at 20° C at pH = 8 after 180 min of irradiation. Error bars indicate standard deviations of the three replicated experiments.

Table 4
Mineralization of TC using different ZnO-based catalysts at 20 °C at different pH after 180 min of irradiation.

Photocatalyst	Sonocatalysis		Photocatalysis		Sonophotocatalysis	
	pH = 6	pH = 8	pH = 6	pH = 8	pH = 6	pH = 8
C0ZO	57.2 ± 0.2	58.1 ± 0.2	18.6 ± 0.3	30.6 ± 0.2	64.1 ± 0.5	65.4 ± 0.2
C1ZO	55.1 ± 0.4	57.0 ± 0.1	69.4 ± 0.1	71.3 ± 0.4	85.5 ± 0.4	86.5 ± 0.2
C2ZO	56.2 ± 0.6	58.2 ± 0.1	94.3 ± 0.2	94.4 ± 0.2	99.8 ± 0.2	99.8 ± 0.1
C3ZO	56.3 ± 0.3	58.1 ± 0.2	79.2 ± 0.3	79.6 ± 0.2	92.7 ± 0.3	93.1 ± 0.3

plausible mechanism for TCs' mineralization was proposed (Fig. 9), one that first involves TCs' hydroxylation and decarbonylation, followed by various degrees of dehydroxylation, ring-opening, demethylation, decarbonylation, and hydroxylation.

3.5. Chemical, sonochemical, photochemical, and sono-photochemical stability of Ca-doped ZnO nanoparticles

Not only does ZnO lose stability at acidic and basic pH levels and thus suffers dissolution, but ZnO-based materials are also sensitive to the action of other external agents such as light and ultrasound, which gives rise to processes of photocorrosion and sonocorrosion. Although those drawbacks often go unconsidered, they are nevertheless relevant for processes that involve using light, ultrasound, or both. In particular, this corrosion tendency inhibits the use of this kind of materials in remediation applications, because it seriously affects their useful lifetime in addition to possible releasing of new pollutants, Zn(II) ions, into the environment. The photocorrosion of ZnO-based materials is supported on the action of holes (Eq. (1)) and enhanced in acidic conditions [57–59].

$$ZnO + 2h^{+}_{vb} \rightarrow Zn^{2+} + \hat{A}\frac{1}{2}O_2 \quad (1)$$

The lesser degree of photodissolution in the alkaline versus acidic mediums could be explained by the greater quantity of OH^- ions, which react with h^{+}_{VB} to form $^{\bullet}OH$ radicals, thereby reducing the dissolution of the ZnO. ZnO is often modified or doped to improve not only photocatalytic activity but also durability by reducing photocorrosion [57–59]. In our experiments, depending on the percentage of Ca dopant, photocorrosion decreased as photooxidation increased (Fig. 10). When photocorrosion, sonocorrosion, and sono-photocorrosion of the analyzed particles were followed in Milli-Q water, in a pH adjusted to 6 or 8 in order to investigate pH's effect, after 48 h of continuous irradiation, the highest value of photocorrosion, as expected, occurred with ZnO without doping, marked by the 56.2% (pH = 6) and 36.4% (pH = 8) dissolution of the photocatalyst. For the doped particles, the lowest value occurred with C3ZO, with 17.9% dissolution of the photocatalyst at pH = 6 and 9.3% dissolution at pH = 8. No trend emerged, however, because the C2ZO catalyst increased its photocorrosion to 33.1% (pH = 6) and 26.1% (pH = 8). Such circumstances complicate pinpointing the best catalyst, because C2ZO, despite presenting the best catalytic performance, also had lower photocorrosion resistance. As expected, photocorrosion was higher in slightly acidic media [60]. Those values are highly promising because, despite the limited amount of data offered in the literature, it is evidenced that Ca doping strongly inhibits photocorrosion compared with other dopants and strategies (Table 6). Some of those outcomes have even been determined in the presence of organic pollutants, which also inhibits photocorrosion (Eq. (1)). In the presence of organic pollutants, holes can react with the pollutants, and as a result, the degradation of organic pollutants competes with photocorrosion,

Table 5
Operational conditions and photocatalytic performance of various catalysts for mineralizing TC.

Catalyst	pH	TC/ ppm	Treatment	Dose/g L^{-1}	Volume/ mL	Light source	Us power	Mineralization/%	Reference
C2ZO	8	10	photocatalysis	0.5	150	1.6 W white LED (2.2 × 10^{-3} W cm^{-2})	–	73.5 (90 min)	This study
C2ZO	8	10	sonophotocatalysis	0.5	150	1.6 W white LED (2.2 × 10^{-3} W cm^{-2})	40 kHz 100 W	99.8 (90 min)	This study
ZnO@MONT	10	120	photocatalysis	0.4	250	50 W Luxten halogen solar simulator	–	94 (75 min)	[1]
Sn-ZnO@PDA/PU	8	20	photocatalysis	2.0	30	500 W Xe lamp (1000 W m^{-2})	–	96.7 (120 min)	[53]
Cu/Cu_2O/CuO-microalgae	8	40	photocatalysis	0.5	250	3 LEDs (6.2 W)	–	94.0 (120 min)	[3]
AgI/$BiVO_4$	n. a.	20	photocatalysis	0.3	100	Xe lamp (300 W)	–	90.5 (120 min)	[54]
Au/B-TiO_2/rGO	n. a.	15	sonophotocatalysis	0.25	40	300 W halogen lamp	40 kHz 600 W	73.6 (60 min)	[55]
TiO_2/MAC	5.5	30	sonophotocatalysis	0.5	500	UV-C lamp, 6 W	20 kHz	50.4 (180 min)	[16]
WO_3/CNT	9	60	sonophotocatalysis	0.7	300	40 W visible lamp	24 kHz 250 W m^{-2}	31.7 (60 min)100% (240 min)	[56]

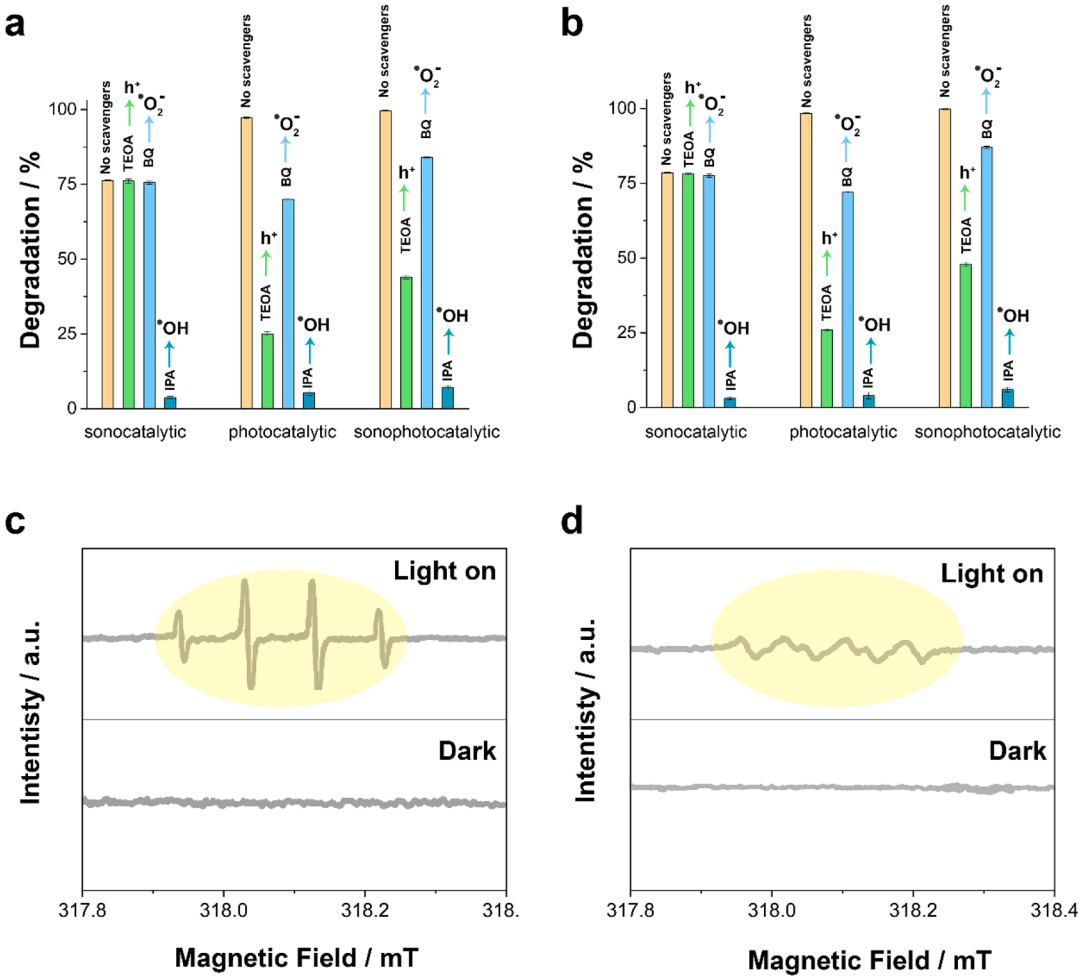

Fig. 8. Trapping of active species during the sonolytic, photocatalytic, and sono-photocatalytic degradation of TC at 20 °C at (a) pH = 6 and (b) pH = 8 after 180 min of LED and/or ultrasound irradiation using 0.5 mg mL^{-1} of the C2ZO catalyst. Error bars indicate standard deviations of the four replicated experiments. EPR spectra of C2ZO with DMPO obtained in dark and visible LED irradiation (c) in aqueous suspension to detect DMPO-$^{\bullet}$OH, and (d) in methanol to detect DMPO-$^{\bullet}O^{2-}$.

thereby suppressing ZnO's dissolution [57]. The enhanced photocatalytic activity of Ca-doped ZnO also indicates that holes can react more effectively with TCs, which translates into the suppression of photocorrosion as more holes are used for degradation and fewer for photocorrosion.

Although the dissolution of ZnO during its irradiation with ultrasound has been observed, to the best of our knowledge no mechanism has been determined to explain that behavior. After 24 h of irradiation with ultrasound and both ultrasound and light, the dissolution of C2ZO was less-approximately 9% (pH = 6) and 6% (pH = 8) for sonocorrosion and approximately 18% (pH = 6) and 7% (pH = 8) for sonophotocorrosion-than in the samples irradiated with light only, which

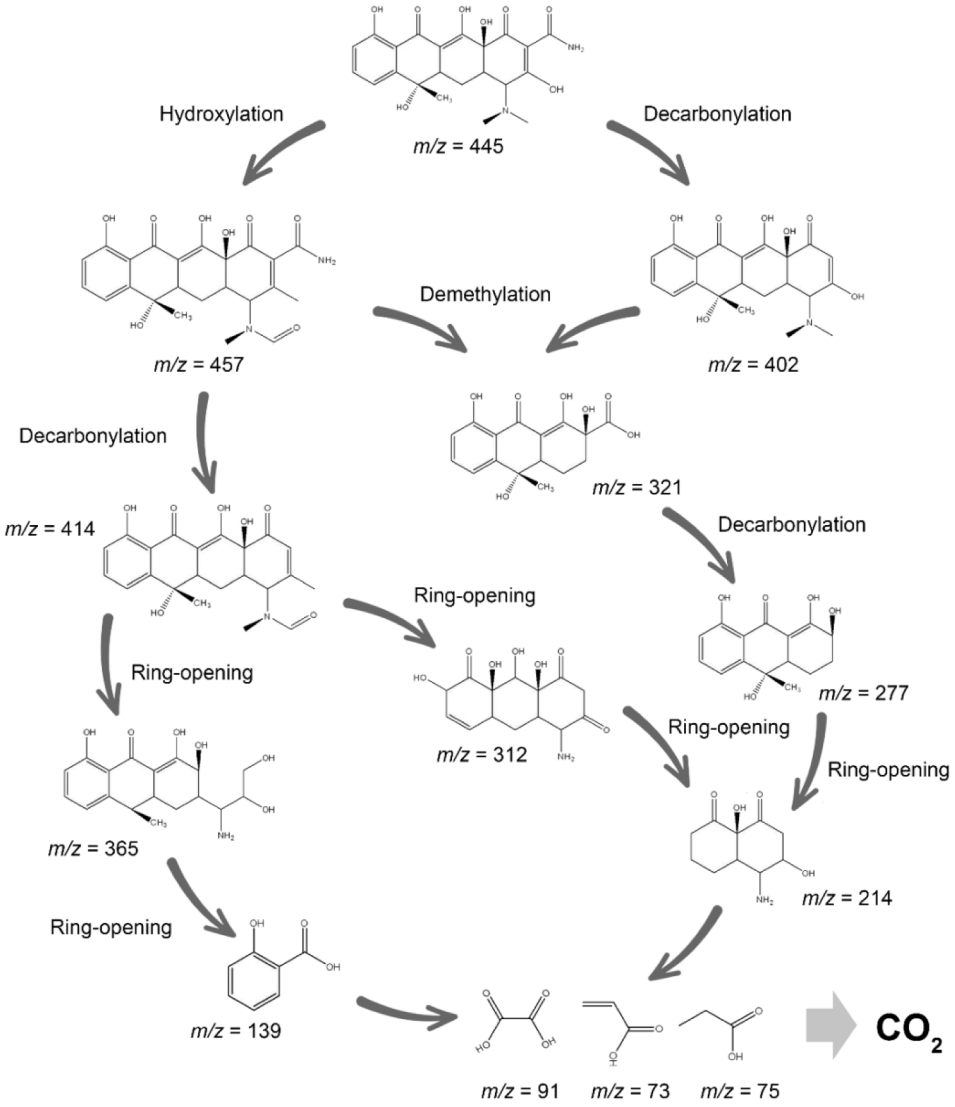

Fig. 9. Viable sono-photocatalytic mineralization pathway of TC using C2ZO as a catalyst.

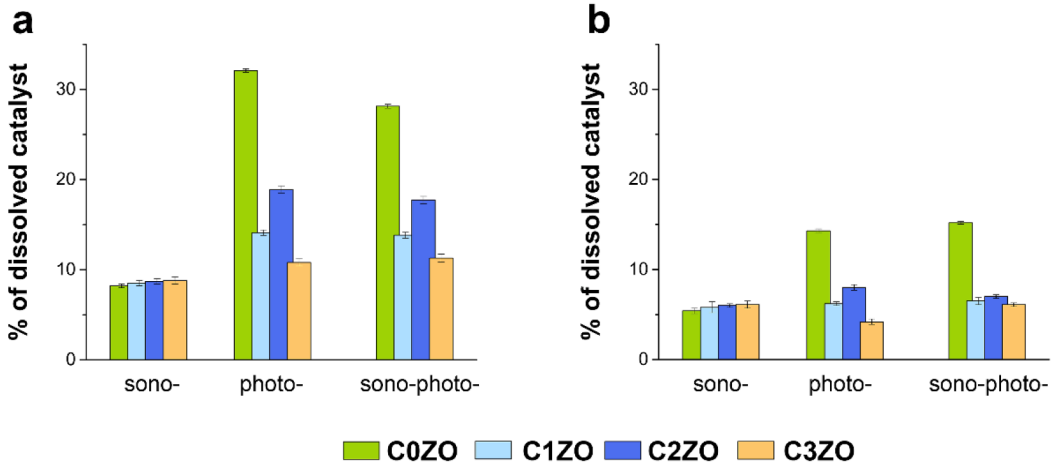

Fig. 10. Time-dependent dissolution of catalyst in presence of ultrasounds, light and both simultaneously at: (a) pH = 6 and (b) pH = 8 at 20 °C. Error bars indicate standard deviations of the four replicated experiments.

Table 6
Photocorrosion activity of ZnO-based materials.

Photocatalyst	Light source	% of dissolved photocatalyst	Irradiation time/h	References
C2ZO	1.6 W white LED (2.2 × 10^{-3} W cm^{-2})	56 (pH = 6)/36 (pH = 8)	48	This study
C3ZO	1.6 W white LED (2.2 × 10^{-3} W cm^{-2})	18 (pH = 6)/9 (pH = 8)	48	This study
Ag-ZnO nanosheets	500 W HP Hg lamp (UV)	12	4	[57]
Fe_3O_4-ZnO@g-C_3N_4	UVC lamp (10 W)	0.6	1.5	[61]
ZnO NPs	Xe lamp (150 mW cm^{-2})	38	1.5	[62]
ZnO/GNP NPs	Xe lamp (150 mW cm^{-2})	27	1.5	[62]
ZnO NRs	Xe lamp (150 mW cm^{-2})	7	1.5	[62]
Al-ZnO	6.2 W white LED (65 mW cm^{-2})	7	40	[60]
ZnO@ZnS	Xe lamp (8 mW cm^{-2})	<2	180	[63]
Ni@ZnO@ZnS	75 W Xe lamp	< 3	160	[64]
Ni-ZnO	75 W Xe lamp	44	48	[43]
ZnO decorated with Ag	75 W Xe lamp	10	48	[43]

dissolved by approximately 19% (pH = 6) and 8% (pH = 8) (Fig. 9). The same trend was observed for all of the catalysts; however, the literature supplies no data to compare the dissolution of the catalyst. Despite the increased production of radicals during sono-photocatalysis, enhancing the formation of more holes, no synergetic effect occurred between the stimuli, the catalyst's dissolution was identical to that obtained in the presence of light only.

To analyze the effect on corrosion processes of the presence of organic pollutants, the C2ZO catalyst's dissolution was analyzed using Milli-Q water at pH = 6 and pH = 8 in the presence and absence of TCs (10 ppm) for 3 h of light irradiation and simultaneous irradiation with ultrasound and light. The catalyst's dissolution in the presence of TC reduced to approximately 15% (pH = 6) and 4% (pH = 8) under light irradiation and to approximately 9% (pH = 6) and 1% (pH = 8) under both light and ultrasound irradiation. Those satisfactory outcomes can be explained by the fact that ultrasound waves facilitate the transport of contaminants to the surface of catalysts and, in the process, clean the catalyst's surface, thereby facilitating the use of holes in the degradation process (i.e., simultaneously reducing holes available to photocorrode ZnO). Therefore, Ca-doped ZnO catalysts are promising candidates for the sono-photocatalytic mineralization of TCs and other organic pollutants with enhanced life-time.

3.6. Reusability

The reusability of two of the catalyst, C2ZO and C3ZO, as sono-photocatalysts was also investigated, given the characteristic's importance for long-term, heterogeneous sono-photocatalysis and, consequently, for their possible strategy's applicability in water decontamination. Fig. 11 illustrates the reusability of these two sono-photocatalysts at pH = 6 and pH = 8.

The results indicate that mineralization did not decrease significantly during 7 consecutive cycles, especially at pH = 8. At pH = 8, reusability seemed much more strong than at pH = 6 and varied less than 1% after continuous working. Those results reinforce the potential use of these Ca-doped ZnO nanopowders for sono-photocatalytic water decontamination.

4. Conclusions

A simple sol–gel process was used to synthesize well-defined Ca-doped ZnO nanopowders with different amounts of Ca in order to achieve morphological, structural, and optoelectronic properties able to promote the sono-photocatalytic mineralization of emerging organic pollutants under visible light irradiation and weak ultrasound stimulation.

The catalyst with Ca amounting to 2 at % had the highest adsorption capacities regardless of the medium's pH. Added to that, 2% Ca-doped ZnO nanopowders exhibited the highest photocatalytic and sono-photocatalytic activity in the mineralization of TC, with mineralization values of at least 90% after 90 min of irradiation with visible light and weak ultrasound stimulation. The effects of pH, light, ultrasound, and catalyst doping were next systematically analyzed to determine the best conditions for the mineralization of TC, which is governed by hydroxyl radicals via a mechanism based on sequential degrees of dehydroxylation, ring opening, demethylation, decarbonylation, and hydroxylation. Although light and ultrasound negatively affect the

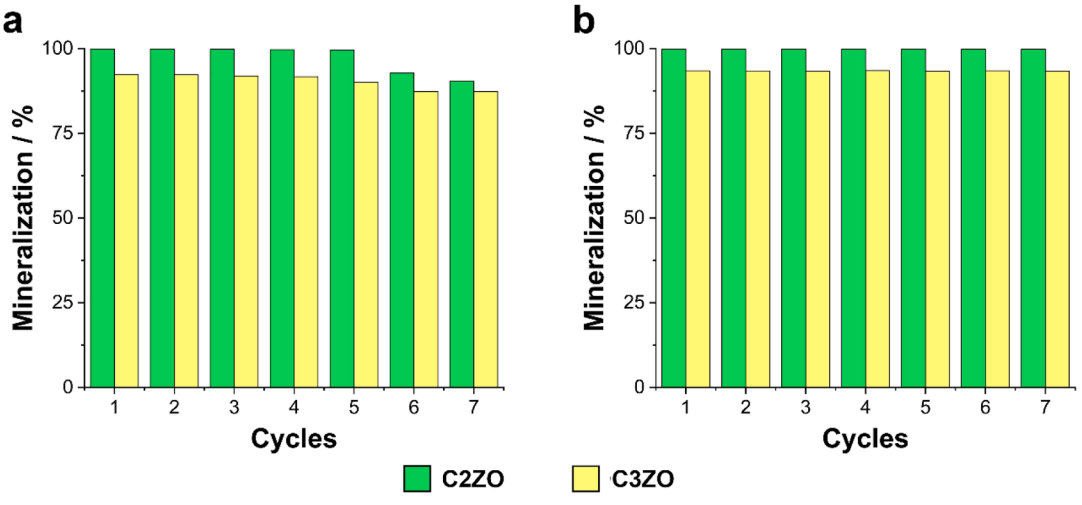

Fig. 11. Reusability of C2ZO and C3ZO nanopowders for mineralizing TC at: (a) pH = 6 and (b) pH = 8 at 20 °C.

catalyst's stability, sono-photocorrosion is minimal in the presence of pollutants—in fact, less than 1% after 3 h of use—which highlights the good reusability of 2% Ca-doped ZnO nanopowders. Altogether, Ca-doped ZnO nanopowders offered meaningful guidance for exploring novel, highly efficient, long-term, eco-friendly catalysts for water decontamination technology.

Declaration of Competing Interest

The authors declare that they have no known competing financial interests or personal relationships that could have appeared to influence the work reported in this paper.

Acknowledgments

This work was supported by the TEC2017-85059-C3-2-R project (cofinanced by the *Fondo Europeo de Desarrollo Regional*, FEDER) from the Spanish M*inisterio de Economía y Competitividad* (MINECO).

References

[1] A. Zyoud, W. Jondi, N. AlDaqqah, S. Asaad, N. Qamhieh, A.R. Hajamohideen, M.H. S. Helal, H. Kwon, H.S. Hilal, Self-sensitization of tetracycline degradation with simulated solar light catalyzed by ZnO@montmorillonite, Solid State Sci. 74 (2017) 131–143, https://doi.org/10.1016/j.solidstatesciences.2017.09.009.

[2] A. Serrà, L. Philippe, F. Perreault, S. Garcia-Segura, Photocatalytic treatment of natural waters. reality or hype? The case of cyanotoxins remediation, Water Res. 188 (2021) 116543, https://doi.org/10.1016/j.watres.2020.116543.

[3] A. Serrà, E. Gómez, J. Michler, L. Philippe, Facile cost-effective fabrication of Cu@Cu_2O@CuO–microalgae photocatalyst with enhanced visible light degradation of tetracycline, Chem. Eng. J. 413 (2021) 127477, https://doi.org/10.1016/j.cej.2020.127477.

[4] S.C. Roberts, T.R. Zembower, Global increases in antibiotic consumption: a concerning trend for WHO targets, Lancet Infect. Dis. 21 (1) (2021) 10–11, https://doi.org/10.1016/S1473-3099(20)30456-4.

[5] T.P. Van Boeckel, E.E. Glennon, D. Chen, M. Gilbert, T.P. Robinson, B.T. Grenfell, S.A. Levin, S. Bonhoeffer, R. Laxminarayan, Reducing antimicrobial use in food animals, Science 357 (6358) (2017) 1350–1352, https://doi.org/10.1126/science.aao1495.

[6] T.P. Van Boeckel, J. Pires, R. Silvester, C. Zhao, J. Song, N.G. Criscuolo, M. Gilbert, S. Bonhoeffer, R. Laxminarayan, Global trends in antimicrobial resistance in animals in low- And middle-income countries, Science 365 (6459) (2019) eaaw1944, https://doi.org/10.1126/science:aaw1944.

[7] R.D.C. Soltani, M. Mashayekhi, M. Naderi, G. Boczkaj, S. Jorfi, M. Safari, Sonocatalytic degradation of tetracycline antibiotic using zinc oxide nanostructures loaded on nano-cellulose from waste straw as nanosonocatalyst, Ultrason. Sonochem. 55 (2019) 117–124, https://doi.org/10.1016/j.ultsonch.2019.03.009.

[8] H. Wang, Y. Wu, M. Feng, W. Tu, T. Xiao, T. Xiong, H. Ang, X. Yuan, J.W. Chew, Visible-light-driven removal of tetracycline antibiotics and reclamation of hydrogen energy from natural water matrices and wastewater by polymeric carbon nitride foam, Water Res. 144 (2018) 215–225, https://doi.org/10.1016/j.watres.2018.07.025.

[9] A.A. Borghi, M.S.A. Palma, Tetracycline: production, waste treatment and environmental impact assessment, Brazilian J. Pharm. Sci. 50 (1) (2014) 25–40, https://doi.org/10.1590/S1984-82502011000100003.

[10] N. Farhadian, R. Akbarzadeh, M. Pirsaheb, T.C. Jen, Y. Fakhri, A. Asadi, Chitosan modified N, S-doped TiO_2 and N, S-doped ZnO for visible light photocatalytic degradation of tetracycline, Int. J. Biol. Macromol. 132 (2019) 360–373, https://doi.org/10.1016/j.ijbiomac.2019.03.217.

[11] C. Ian, R. Marilyn, Tetracycline antibiotics: mode of action, applications, molecular biology, and epidemiology of bacterial resistance, Microbiol. Mol. Biol. Rev. 65 (2001) 232–260, https://doi.org/10.1128/MMBR.65.2.232.

[12] Y. Cui, X. Zhang, H. Zhang, Q. Cheng, X. Cheng, Construction of BiOCOOH/g-C_3N_4 composite photocatalyst and its enhanced visible light photocatalytic degradation of amido black 10B, Sep. Purif. Technol. 210 (2019) 125–134, https://doi.org/10.1016/j.seppur.2018.07.059.

[13] R. Andreozzi, V. Caprio, et al., Advanced oxidation processes (AOP) for water purification and recovery, Catal. Today. 53 (1999) 51–59.

[14] M.A. Oturan, J.-J. Aaron, Advanced oxidation processes in water/wastewater treatment: Principles and applications. a review, Crit. Rev. Environ. Sci. Technol. 44 (23) (2014) 2577–2641, https://doi.org/10.1080/10643389.2013.829765.

[15] R. Artal, L. Philippe, E. Gómez, A. Serrà, Recycled cyanobacteria ashes for sono-enhanced photo-Fenton wastewater decontamination, J. Clean. Prod. 267 (2020) 121881, https://doi.org/10.1016/j.jclepro.2020.121881.

[16] B. Kakavandi, N. Bahari, R. Rezaei Kalantary, E. Dehghani Fard, Enhanced sono-photocatalysis of tetracycline antibiotic using TiO_2 decorated on magnetic activated carbon (MAC@T) coupled with US and UV: a new hybrid system, Ultrason. Sonochem. 55 (2019) 75–85, https://doi.org/10.1016/j.ultsonch.2019.02.026.

[17] R. Yang, Z. Wu, Y. Yang, Y. Li, L. Zhang, B. Yu, Understanding the origin of synergistic catalytic activities for ZnO based sonophotocatalytic degradation of methyl orange, J. Taiwan Inst. Chem. Eng. 119 (2021) 128–135, https://doi.org/10.1016/j.jtice.2021.01.028.

[18] E. Selli, Synergistic effects of sonolysis combined with photocatalysis in the degradation of an azo dye, Phys. Chem. Chem. Phys. 4 (2002) 6123–6128, https://doi.org/10.1039/b205881b.

[19] P. Gholami, A. Khataee, R.D.C. Soltani, A. Bhatnagar, A review on carbon-based materials for heterogeneous sonocatalysis: fundamentals, properties and applications, Ultrason. Sonochem. 58 (2019) 104681, https://doi.org/10.1016/j.ultsonch.2019.104681.

[20] D. Spasiano, R. Marotta, S. Malato, P. Fernandez-Ibañez, I. Di Somma, Solar photocatalysis: materials, reactors, some commercial, and pre-industrialized applications. a comprehensive approach, Appl. Catal. B Environ. 170–171 (2015) 90–123, https://doi.org/10.1016/j.apcatb.2014.12.050.

[21] M.R. Hoffmann, S.T. Martin, W. Choi, D.W. Bahnemann, Environmental Applications of Semiconductor Photocatalysis 95 (1) (1995) 69–96, https://doi.org/10.1021/cr00033a004.

[22] L.K.B. Paragas, V. Dien Dang, R.S. Sahu, S. Garcia-Segura, M.D.G. de Luna, J.A. I. Pimentel, R.-A. Doong, Enhanced visible-light-driven photocatalytic degradation of acetaminophen over CeO_2/I, K-codoped C_3N_4 heterojunction with tunable properties in simulated water matrix, Sep. Purif. Technol. 272 (2021) 117567, https://doi.org/10.1016/j.seppur.2020.117567.

[23] E. Brillas, A. Serrà, S. Garcia-Segura, Biomimicry designs for photoelectrochemical systems: strategies to improve light delivery efficiency, Curr. Opin. Electrochem. 26 (2021) 100660, https://doi.org/10.1016/j.coelec.2020.100660.

[24] A.A. Peyghan, M. Noei, The alkali and alkaline earth metal doped ZnO nanotubes: DFT studies, Phys. B Condens. Matter. 432 (2014) 105–110, https://doi.org/10.1016/j.physb.2013.09.051.

[25] A. Rosset, K. Djessas, V. Goetz, S. Grillo, G. Plantard, Sol-gel synthesis and solar photocatalytic activity of Ca-alloyed ZnO nanoparticles elaborated using different precursors, RSC Adv. 10 (43) (2020) 25456–25466, https://doi.org/10.1039/C9RA10131D.

[26] A.G. Oliveira, J.d.L. Andrade, M.C. Montanha, S.M. Lima, L.H.d.C. Andrade, A. A. Winkler Hechenleitner, E.A.G. Pineda, D.M.F.d. Oliveira, Decontamination and disinfection of wastewater by photocatalysis under UV/visible light using nano-catalysts based on Ca-doped ZnO, J. Environ. Manage. 240 (2019) 485–493, https://doi.org/10.1016/j.jenvman.2019.03.124.

[27] M. Qi, Q. Hou, S. Sha, M. Chen, First-principles of Be/Mg/Ca doping and point defects of V_{Zn} and H_i in the magnetic and optical properties of ZnO, Mater. Sci. Semicond. Process. 131 (2021) 105857, https://doi.org/10.1016/j.mssp.2021.105857.

[28] C.Y. Ma, J.Y. Xu, X.J. Liu, Decomposition of an azo dye in aqueous solution by combination of ultrasound and visible light, Ultrasonics. 44 (2006) 375–378, https://doi.org/10.1016/j.ultras.2006.05.164.

[29] B. Neppolian, L. Ciceri, C.L. Bianchi, F. Grieser, M. Ashokkumar, Sonophotocatalytic degradation of 4-chlorophenol using Bi_2O_3/$TiZrO_4$ as a visible light responsive photocatalyst, Ultrason. Sonochem. 18 (1) (2011) 135–139, https://doi.org/10.1016/j.ultsonch.2010.04.002.

[30] C.E. Säbel, J.M. Neureuther, S. Siemann, A spectrophotometric method for the determination of zinc, copper, and cobalt ions in metalloproteins using Zincon, Anal. Biochem. 397 (2) (2010) 218–226, https://doi.org/10.1016/j.ab.2009.10.037.

[31] Y. Chen, D.M. Bagnall, H.J. Koh, K.T. Park, K. Hiraga, Z. Zhu, T. Yao, Plasma assisted molecular beam epitaxy of ZnO on c-plane sapphire: growth and characterization, J. Appl. Phys. 84 (1998) 3912–3918, https://doi.org/10.1063/1.368595.

[32] D.R. Kulkarni, S.J. Malode, K. Keerthi Prabhu, N.H. Ayachit, R.M. Kulkarni, N. P. Shetti, Development of a novel nanosensor using Ca-doped ZnO for antihistamine drug, Mater. Chem. Phys. 246 (2020) 122791, https://doi.org/10.1016/j.matchemphys.2020.122791.

[33] S. Umavathi, M.S. AlSalhi, S. Devanesan, S. Kadhiravan, K. Gopinath, M. Govindarajan, Synthesis and characterization of ZnO and Ca-ZnO nanoparticles for potential antibacterial activity and plant micronutrients, Surfaces and Interfaces. 21 (2020) 100796, https://doi.org/10.1016/j.surfin.2020.100796.

[34] I. Ahmad, E. Ahmed, M. Ahmad, M.S. Akhtar, M.A. Basharat, W.Q. Khan, M. I. Ghauri, A. Ali, M.F. Manzoor, The investigation of hydrogen evolution using Ca doped ZnO catalysts under visible light illumination, Mater. Sci. Semicond. Process. 105 (2020) 104748, https://doi.org/10.1016/j.mssp.2019.104748.

[35] G.K. Williamson, W.H. Hall, Discussion of the theories of line broadening, Acta Metall. 1 (1953) 22, https://doi.org/10.1016/0001-6160(53)90006-6.

[36] J.I. Langford, A.J.C. Wilson, Scherrer after sixty years: a survey and some new results in the determination of crystallite size, J. Appl. Crystallogr. 11 (2) (1978) 102–113, https://doi.org/10.1107/S0021889878012844.

[37] V. Uvarov, I. Popov, Metrological characterization of X-ray diffraction methods at different acquisition geometries for determination of crystallite size in nano-scale materials, Mater. Charact. 85 (2013) 111–123, https://doi.org/10.1016/j.matchar.2013.09.002.

[38] C. Karthikeyan, L. Arun, A.S.H. Hameed, K. Gopinath, L. Umaralikahan, G. Vijayaprasath, P. Malathi, Structural, optical, thermal and magnetic properties of nickel calcium and nickel iron co-doped ZnO nanoparticles, J. Mater. Sci. Mater. Electron. 30 (9) (2019) 8097–8104, https://doi.org/10.1007/s10854-019-01160-z.

[39] S.B. Khan, H.M. Marwani, A.M. Asiri, E.M. Bakhsh, Exploration of calcium doped zinc oxide nanoparticles as selective adsorbent for extraction of lead ion, Desalin.

Water Treat. 57 (41) (2016) 19311–19320, https://doi.org/10.1080/19443994.2015.1109560.
[40] W. Gu, D.W. Bousfield, C.P. Tripp, Formation of calcium carbonate particles by direct contact of $Ca(OH)_2$ powders with supercritical CO_2, J. Mater. Chem. 16 (2006) 3312–3317, https://doi.org/10.1039/b607184h.
[41] A.-I. Istrate, F. Nastase, I. Mihalache, F. Comanescu, R. Gavrila, O. Tutunaru, C. Romanitan, V. Tucureanu, M. Nedelcu, R. Müller, Synthesis and characterization of Ca doped ZnO thin films by sol–gel method, J. Sol-Gel Sci. Technol. 92 (3) (2019) 585–597, https://doi.org/10.1007/s10971-019-05144-7.
[42] A.S.H. Hameed, C. Karthikeyan, S. Sasikumar, V. Senthil Kumar, S. Kumaresan, G. Ravi, Impact of alkaline metal ions Mg^{2+}, Ca^{2+}, Sr^{2+} and Ba^{2+} on the structural, optical, thermal and antibacterial properties of ZnO nanoparticles prepared by the co-precipitation method, J. Mater. Chem. B. 1 (2013) 5950–5962, https://doi.org/10.1039/c3tb21068e.
[43] A. Serrà, Y. Zhang, B. Sepúlveda, E. Gómez, J. Nogués, J. Michler, L. Philippe, Highly active ZnO-based biomimetic fern-like microleaves for photocatalytic water decontamination using sunlight, Appl. Catal. B Environ. 248 (2019) 129–146, https://doi.org/10.1016/j.apcatb.2019.02.017.
[44] R. Al-Gaashani, S. Radiman, A.R. Daud, N. Tabet, Y. Al-Douri, XPS and optical studies of different morphologies of ZnO nanostructures prepared by microwave methods, Ceram. Int. 39 (3) (2013) 2283–2292, https://doi.org/10.1016/j.ceramint.2012.08.075.
[45] W. Yu, D. Han, G. Cui, Y. Cong, J. Dong, X. Zhang, X. Zhang, Y.i. Wang, S. Zhang, High-performance calcium-doped zinc oxide thin-film transistors fabricated on glass at low temperature, Jpn. J. Appl. Phys. 55 (4S) (2016) 04EK05, https://doi.org/10.7567/JJAP.55.04EK05.
[46] F. Pantò, S.G. Leonardi, E. Fazio, P. Frontera, A. Bonavita, G. Neri, P. Antonucci, F. Neri, S. Santangelo, CO_2 sensing properties of electro-spun Ca-doped ZnO fibres, Nanotechnology. 29 (30) (2018) 305501, https://doi.org/10.1088/1361-6528/aac27c.
[47] L. El Mir, Luminescence properties of calcium doped zinc oxide nanoparticles, J. Lumin. 186 (2017) 98–102, https://doi.org/10.1016/j.jlumin.2017.02.029.
[48] M. Liu, L.-a. Hou, S. Yu, B. Xi, Y. Zhao, X. Xia, MCM-41 impregnated with A zeolite precursor: synthesis, characterization and tetracycline antibiotics removal from aqueous solution, Chem. Eng. J. 223 (2013) 678–687, https://doi.org/10.1016/j.cej.2013.02.088.
[49] H. Wang, C. Fang, Q. Wang, Y. Chu, Y. Song, Y. Chen, X. Xue, Sorption of tetracycline on biochar derived from rice straw and swine manure, RSC Adv. 8 (29) (2018) 16260–16268, https://doi.org/10.1039/C8RA01454J.
[50] J. Rivera-Utrilla, C.V. Gómez-Pacheco, M. Sánchez-Polo, J.J. López-Peñalver, R. Ocampo-Pérez, Tetracycline removal from water by adsorption/bioadsorption on activated carbons and sludge-derived adsorbents, J. Environ. Manage. 131 (2013) 16–24, https://doi.org/10.1016/j.jenvman.2013.09.024.
[51] M. Gouamid, M.R. Ouahrani, M.B. Bensaci, Adsorption equilibrium, kinetics and thermodynamics of methylene blue from aqueous solutions using date palm Leaves, Energy Procedia. 36 (2013) 898–907, https://doi.org/10.1016/j.egypro.2013.07.103.
[52] H. Ibrahim, H. de Lasa, Photo-catalytic degradation of air borne pollutants apparent quantum efficiencies in a novel photo-CREC-air reactor, Chem. Eng. Sci. 58 (3-6) (2003) 943–949, https://doi.org/10.1016/S0009-2509(02)00632-2.
[53] Z. Liu, X. Cai, S. Fan, Y. Zhang, H. Hu, Z. Huang, J. Liang, Y. Qin, Preparation of a stable polyurethane sponge supported Sn-doped ZnO composite via double-template-regulated bionic mineralization for visible-light-driven photocatalytic degradation of tetracycline, J. Environ. Chem. Eng. 9 (4) (2021) 105541, https://doi.org/10.1016/j.jece:2021.105541.
[54] F. Chen, Q.i. Yang, J. Sun, F. Yao, S. Wang, Y. Wang, X. Wang, X. Li, C. Niu, D. Wang, G. Zeng, Enhanced photocatalytic degradation of tetracycline by AgI/$BiVO_4$ heterojunction under visible-light irradiation: mineralization efficiency and mechanism, ACS Appl. Mater. Interfaces. 8 (48) (2016) 32887–32900, https://doi.org/10.1021/acsami.6b12278.
[55] V. Vinesh, A.R.M. Shaheer, B. Neppolian, Reduced graphene oxide (rGO) supported electron deficient B-doped TiO_2 (Au/B-TiO_2/rGO) nanocomposite: an efficient visible light sonophotocatalyst for the degradation of Tetracycline (TC), Ultrason. Sonochem. 50 (2019) 302–310, https://doi.org/10.1016/j.ultsonch.2018.09.030.
[56] A.A. Isari, M. Mehregan, S. Mehregan, F. Hayati, R. Rezaei Kalantary, B. Kakavandi, Sono-photocatalytic degradation of tetracycline and pharmaceutical wastewater using WO_3/CNT heterojunction nanocomposite under US and visible light irradiations: a novel hybrid system, J. Hazard. Mater. 390 (2020) 122050, https://doi.org/10.1016/j.jhazmat.2020.122050.
[57] X. Ma, H. Li, T. Liu, S. Du, Q. Qiang, Y. Wang, S. Yin, T. Sato, Comparison of photocatalytic reaction-induced selective corrosion with photocorrosion: Impact on morphology and stability of Ag-ZnO, Appl. Catal. B Environ. 201 (2017) 348–358, https://doi.org/10.1016/j.apcatb.2016.08.029.
[58] J. Liu, P. Wang, W. Qu, H. Li, L. Shi, D. Zhang, Nanodiamond-decorated ZnO catalysts with enhanced photocorrosion-resistance for photocatalytic degradation of gaseous toluene, Appl. Catal. B Environ. 257 (2019) 117880, https://doi.org/10.1016/j.apcatb.2019.117880.
[59] Y. Zhao, J. Ma, J. Liu, Y. Bao, Synthesis of fireworks-shaped ZnO/graphite-like carbon nanowires with enhanced visible-light photocatalytic activity and anti-photocorrosion, Colloids Surfaces A Physicochem. Eng. Asp. 518 (2017) 57–63, https://doi.org/10.1016/j.colsurfa.2016.12.050.
[60] M. Benamara, E. Gómez, R. Dhahri, A. Serrà, Enhanced Photocatalytic Removal of Cyanotoxins by Al-Doped ZnO Nanoparticles with Visible-LED Irradiation, Toxins (Basel). 13 (1) (2021) 66, https://doi.org/10.3390/toxins13010066.
[61] A. Mirzaei, Z. Chen, F. Haghighat, L. Yerushalmi, Hierarchical magnetic petal-like Fe_3O_4-ZnO@g-C_3N_4 for removal of sulfamethoxazole, suppression of photocorrosion, by-products identification and toxicity assessment, Chemosphere. 205 (2018) 463–474, https://doi.org/10.1016/j.chemosphere.2018.04.102.
[62] M. Tayebi, A. Tayyebi, Z. Masoumi, B.-K. Lee, Photocorrosion suppression and photoelectrochemical (PEC) enhancement of ZnO via hybridization with graphene nanosheets, Appl. Surf. Sci. 502 (2020) 144189, https://doi.org/10.1016/j.apsusc.2019.144189.
[63] A. Serrà, L. Philippe, Simple and scalable fabrication of hairy ZnO@ZnS core@shell Cu cables for continuous sunlight-driven photocatalytic water remediation, Chem. Eng. J. 401 (2020) 126164, https://doi.org/10.1016/j.cej.2020.126164.
[64] A. Serrà, R. Artal, J. García-Amorós, B. Sepúlveda, E. Gómez, J. Nogués, L. Philippe, Hybrid Ni@ZnO@ZnS-microalgae for circular economy: a smart route to the efficient integration of solar photocatalytic water decontamination and bioethanol production, Adv. Sci. 7 (3) (2020) 1902447, https://doi.org/10.1002/advs.v7.310.1002/advs.201902447.